UNIVERSITÄT
BAYREUTH

DISSERTATION

Permanent Magnet Ensembles
—
Field Properties and Dynamic Interaction

STEFAN HARTUNG

Permanent Magnet Ensembles
—
Field Properties and Dynamic Interaction

Von der Universität Bayreuth
zur Erlangung des Grades eines
Doktors der Naturwissenschaften (Dr. rer. nat.)
genehmigte Abhandlung

von

STEFAN HARTUNG

geboren in Nürnberg

1. Gutachter: Prof. Dr. Ingo Rehberg
2. Gutachter: Prof. Dr. Matthias Weiss

Tag der Einreichung: 31. August 2021
Tag des Kolloquiums: 07. Dezember 2021

Kurzdarstellung

Diese Arbeit befasst sich in drei Projekten mit bemerkenswerten Eigenschaften von Permanentmagneten auf unterschiedlichen Größenskalen und deren potentiellen Nutzen.

Im ersten Teil wird die Größenverteilung von permanentmagnetischen Nanopartikeln untersucht, welche die Bestandteile eines Ferrofluids bilden. Für diese Untersuchung wird die Methode der grafischen Rektifizierung von Magnetisierungskurven eingeführt und genutzt, um die experimentellen Daten von zwei verschiedenen Ferrofluiden auszuwerten. Mit dieser Methode lassen sich das arithmetische und das geometrische Mittel der magnetischen Momente direkt graphisch ablesen, ohne dass eine Annahme über die zugrundeliegende Verteilungsfunktion erforderlich ist. Es ist festzustellen, dass Langevin-Funktionen, Gamma-Verteilungen und Lognormal-Verteilungen mit Fitparametern die gemessenen Funktionen alle gleich gut interpolieren können: Dies ist eine Manifestation des schlecht gestellten inversen Problems. Für den praktischen Gebrauch empfehlen wir nachdrücklich die Superposition einer Handvoll Langevin-Funktionen.

Die Feldeigenschaften eines Ensembles von Dipolen sind Gegenstand des zweiten Projekts. Das Zusammenbringen von acht kugelförmigen Permanentmagneten zu einer Würfelform lässt die magnetischen Momente in ein Kontinuum von Gleichgewichtslagen relaxieren. Es wird erstmals experimentell gezeigt, dass das magnetische Fernfeld eines solchen Würfels mit der siebten Potenz des Abstandes abnimmt und damit in niedrigster Ordnung einen Dotriakontapol formt. Zudem entsteht durch die unendlichfache Entartung der Dipolausrichtungen in diesem Zustand eine siebenfache rastmomentfreie Kupplung zwischen den Magneten.

Eine geometrisch einfachere rastmomentfreie Permanentmanget-Kupplung wird im dritten Projekt anhand von zwei kugelförmigen Neodym-Eisen-Bor-Magneten untersucht. Der experimentelle Aufbau ermöglicht die Realisierung einer rastmomentfreien Kupplung, wobei ein Magnet von einem Schrittmotor getrieben wird und den anderen durch rein magnetische Wechselwirkung antreibt. Die Punktdipoleigenschaft des Außenfeldes dieser Kugelmagneten wird experimentell sehr gut bestätigt. Das dynamische Verhalten dieses Aufbaus wird zum ersten Mal experimentell untersucht. Es wird ein mathematisches Modell erstellt, dessen numerische Integration die experimentellen Daten gut beschreibt. Diese Ergebnisse sind teilweise bereits publiziert und werden teilweise in der Einleitung dieser Arbeit erstmals vorgestellt.

Abstract

This work deals with remarkable features of permanent magnets on different length scales and the possibilities of their technical implementation over three different projects.

In the first part the size distribution of permanent magnet nanoparticles is studied when constituting a ferrofluid. For this investigation the method of graphical rectification of magnetization curves is introduced and used for the evaluation of experimental data of two different fluids. With this method a direct graphical readout of the arithmetic and harmonic mean of the magnetic moments is possible, without the need for an assumption of the underlying distribution function. It is noted that Langevin functions, Gamma distributions and Lognormal distributions are all able to interpolate the data equally well: This is a manifestation of this ill-posed inverse problem. For practical implementation, we recommend the use of a superposition of a handful of Langevin functions.

The field properties of an ensemble of dipoles are the scope of the second project. The gathering of eight spherical permanent magnets in a cubic formation leads to a relaxation of the magnetic moments into a continuum of equilibrium positions. It is shown experimentally for the first time that the far field of such a cube decreases with the seventh order of the distance, forming a dotriacontapole in its lowest order. In addition, the infinite frustration of the dipole orientations forms a seven-fold cogging-free coupling between the magnets.

A cogging-free coupling with simpler geometry is investigated in the third project under the use of two spherical magnets out of a neodymium iron bor alloy. The experimental setup makes the implementation of a cogging-free coupling possible while one magnet is driven by a stepper motor and is itself driving the other magnet purely by magnetic interaction. The point dipole feature of the far field of these spherical magnets is confirmed well experimentally. The dynamic behavior of this setup is studied experimentally for the first time. A mathematical model is created whose numerical integration is in good accordance with the experimental data. A part of the results can be found in the corresponding publication while another part of the results is presented in the introductory part of this work for the first time.

Contents

Kurzdarstellung V

Abstract VII

Contents IX

I Outline of Results 1

1 Introduction 3

2 Analyzing the Size Distribution of Magnetic Nanoparticles in Suspension 5

3 Forming a Dotriacontapole from eight spherical permanent magnets 9

4 Special Features of Permanent Magnet Couplings 13

Bibliography 21

List of Publications 23

II Publications 25

1 Measuring magnetic moments of polydisperse ferroluids utilizing the inverse Langevin function 27

2 Graphical Magnetogranulometry of EMG909 35

3 Assembly of eight spherical magnets into a dotriacontapole configuration 41

4 Dynamics of a magnetic gear with two cogging-free operation modes 49

Acknowledgments 65

Eidesstattliche Versicherung 67

Part I

Outline of Results

1 Introduction

Magnets have a long tradition of being part of our daily lives and reportedly were already known to the ancient Greeks. They coined the term "magnet", according to a finding place of magnetite called Magnesia in Anatolia (Carus, 2019). They realized that a special kind of rock – we know it as magnetite or lodestone today – was able to attract small amounts of iron and other lodestones. Similar discoveries were documented in ancient India and China. Even though an obscure understanding of this experienced attraction – spirits and gods that command the lodestones to their actions – was present at that time, it had been put to practical use over the centuries. In India, a first medical implementation for magnetic materials was found with lodestones that could extract iron splinters and arrow heads from wounds (Bhishagratna, 2006). In the middle ages, Chinese were the first to develop a magnetic version of a compass with a small "fish" out of magnetized iron that was made afloat in a bowl of water (Needham *et al.*, 1976).

Centuries later, the development of electromagnetism shed light on the underlying mechanisms of magnetism, directly expanding the variety of implementations (Bergmann *et al.*, 2006). This is even more relevant today, where we drive electric cars, magnetic valves secure the water supply of the automatic washing machine, mobile communication using electromagnetic waves is ubiquitous, and our complete cultural heritage is being digitized and stored on magnetic hard discs at steadily decreasing length scales.

When permanent magnets in the form of nanoparticles are suspended in a fluid, the result is called a ferrofluid (Rosensweig, 2013; Stephen, 1965). The magnetic moments of these particles scale with their respective size. They are coated to avoid agglomeration and with this appear at a size of 10 nm or less. Since the coating of the nanoparticles wears out over time, the particle size distribution is an important quality factor of a ferrofluid. To access this feature, a magnetization curve of such a fluid can be analyzed. However, traditionally one had to determine the underlying distribution function of the particles within the fluid first, which is hard to obtain. In the first part of this work, a new method is presented, that is able to reliably extract key values of the underlying particle size distribution without assuming a specific distribution function.

Most permanent magnets can in lowest order be described as magnetic dipoles. Pure higher order multipoles are rare to find. By forming clusters of magnetic dipoles with certain geometries, true multipoles can be created. Such a geometric formation that yields a magnetic dotriacontapole is examined in some detail in the second part of this work.

Even the investigation of the interaction of two single dipoles can lead to fruitful novel results. The contact-free drive of one magnet by another magnet is already commonly used in technical applications, most prominently maybe the stir fry in chemistry labs. The use of two permanent magnets of spherical shape opens up new possibilities – due to their close resemblance to perfect magnetic dipoles. By applying the right geometry, these magnets can form a novel cogging-free clutch. Cogging-free operation is a feature highly sought after in magnetically driven machines. In the third part of this work, the dynamic limits of such a coupling and its geometric deviations are investigated for the first time, unraveling several classes of operation modes and their transitions.

2 Analyzing the Size Distribution of Magnetic Nanoparticles in Suspension

Publications 1 and 2 featured in this work focus on analyzing the dipole strength of magnetic particles in a ferrofluid. This is achieved by a graphical rectification of their respective magnetization curves — a method that can be expanded beyond the scope of ferrofluids towards any particles with a dipole moment in a fluid.

In general, the size and dipole strength of magnetic nanoparticles in suspension are described by certain distribution functions. While several of these are commonly used to describe ferrofluid compositions, it is shown by Ivanov *et al.* (2007) that the choice among them has a strong influence on the information that can be obtained from a data set. Unfortunately, determining the correct distribution function of a given magnetization curve is challenging because of the ill-posed character of this problem. This is visible in the top panel in Fig. 3 of publication 1 where two of the most commonly used distribution functions, a gamma and a log-normal distribution, are compared to a bidisperse delta distribution. Even though these functions are fundamentally different, their resulting magnetization curves are hardly distinguishable.

With our method of graphical rectification, we are able to obtain several statistical relevant values without having to choose a specific distribution function. Taking the first derivative to the effective magnetic flux density of the inverse Langevin function of the magnetization curve, flattens the typical s-shape of these curves, as shown in the bottom panel of Fig. 3 in publication 1. Most importantly though, two statistical key values can be read out safely from the rectified graph. As visualized in Fig. 2 of publication 1, the limit value for large effective magnetic fields shows the harmonic mean of the magnetic moments, and for vanishing effective fields the arithmetic mean of the moments becomes directly visible as the maximum value.

Even though the advantage of independence from a certain distribution function is evident, there is still one variable that has to be determined with high precision for graphical magnetogranulometry: the saturation magnetization of the fluid. To obtain this, two options have proven to be successful.

In the first option, we plot the magnetization data against the inverse effective magnetic flux density. An asymptotic polynomial fit towards vanishing inverse flux densities then yields the value of the saturation magnetization as shown exemplary in Fig. 2.1.

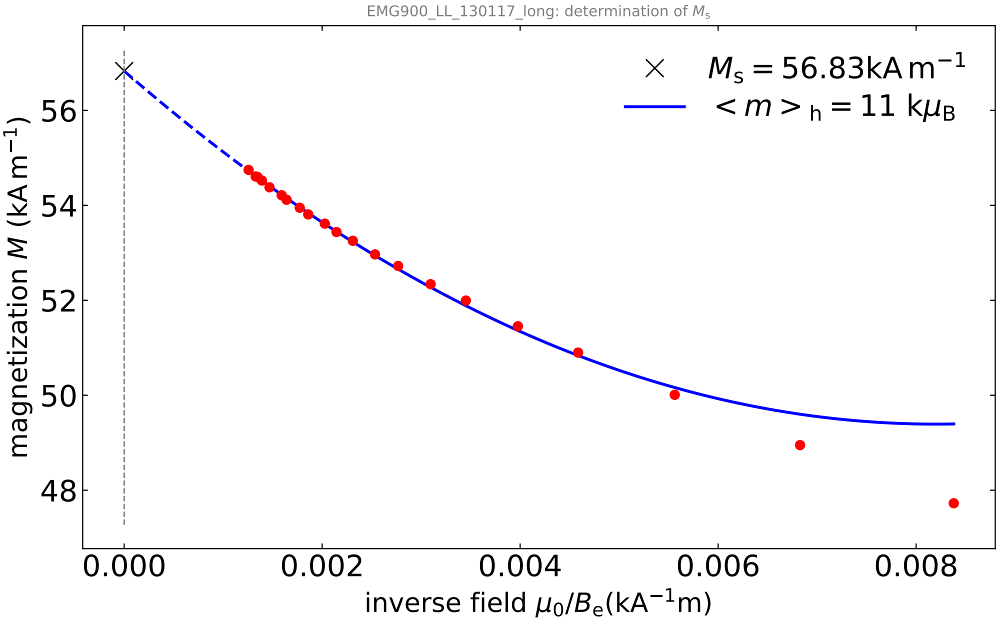

Figure 2.1: Asymptotic fit to inverted effective magnetic field data to obtain the saturation magnetization of a ferrofluid.

In the second option, a fit to the magnetization curves according to any distribution function can be used to calculate the saturation magnetization as its limit value. We find that a quadmodal sum of Langevin curves is most practical to interpolate a given data set, as discussed in publication 2. There we show the reliability of this fitting method for data interpolation and its revelation of the saturation magnetization. We are aware though that such a discrete function itself can not give reliable information for the dipole strength distributions of most ferrofluids which generally have to be assumed to be continuous.

However, there are systems in which the contained magnetic particles can all be divided into few, highly distinguishable parties. One example for this gives the work of Taheri *et al.* (2015) in which the self-assembly of nanoparticles in solution into highly ordered chains, sheets and cuboids has been discovered, once an external magnetic field is applied. Another example are studies on the field of magnetotactic bacteria. These organisms have the ability to synthesize crystal-like permanent magnetic nanoparticles within their body, so-called magnetosomes. They are aligned in a chain along the main axis of the bacteria which use them for orientation along earth's magnetic field. These particles are of highly consistent size and dipole strength. For this and their natural, bio-friendly generation by the bacteria, magnetosomes are a key research interest with focus on their bio-medical application (Alphandéry, 2014; Araujo *et al.*, 2015; Jacob & Suthindhiran, 2016; Yan *et al.*, 2012). In recent years, the controlled cultivation of these organisms and the extraction of their magnetosomes has been established at the University of Bayreuth (Mickoleit *et al.*, 2018). As a current project in our research group, under the lead of Reinhard Richter, the magnetization curves of a dilute suspension of living and dead magnetotactic bacteria in water are investigated. Since the dipole strength of the magnetosomes is highly quantized, a multimodal fit of discrete Langevin curves could be able to identify different chain lengths and singular magnetosomes in the solution.

Apart from the magnetic dipole moments, a sum of Langevin curves also accounts for the temperature within a fluid. While this is less interesting for common ferrofluids, it provides us with another challenge for future research on magnetotactic bacteria. Once the magnetization curve of a suspension of living organisms can be compared to itself after all bacteria have died without a change in their composition of magnetosome chain lengths, an effective temperature difference could be calculated between the living and dead sample. Even though this value will not show the actual rise in temperature that comes with the presence of living organisms, it could provide a reliable tool to measure the presence of life from a single magnetization curve.

3 Forming a Dotriacontapole from eight spherical permanent magnets

In the previous chapter, we briefly shed light on the clustering dynamics of magnetic nanoparticles in suspension under the influence of an external magnetic field. As shown by Taheri *et al.* (2015), cuboidal particles can form chains, sheets and simple cubic superlattices, once an external magnetic field is applied, that can even remain stable once the field is turned off. These supercubes appear to be the final state of the clustering dynamics. While they can contain more than 10000 particles (Taheri *et al.*, 2015), the attraction of the cuboids towards each other seems comparably small. This raises the question about the orientation of the individual dipole moments of the particles inside the cube. While the linear orientation of the dipoles inside a chain is clear, and the division into parallel and antiparallel orientation for chains that form a sheet can also be well understood, the orientation of dipoles in a cubic arrangement follows no intuitive order: As seen in a simulation of a stable equilibrium state of a of 5 x 5 x 5 cubic cluster of point dipoles in Fig. 4 of the work of Taheri *et al.* (2015), the dipoles can be completely asymmetrically aligned. Also, this is only one of a manifold of stable solutions for the dipole orientations. Schönke *et al.* (2015) provide an upper bound S_{max} for the total number of equilibrium solutions of an assembly of N dipoles as

$$S_{\mathrm{max}} = 2^{3N} \tag{3.1}$$

This leads to a staggering high number of possible equilibria for the 5 x 5 x 5 example of $S_{\mathrm{max}} = 2^{375}$, which makes a numerical investigation of all solutions infeasible with todays computational tools. Also, any experimental approach would surely show a tremendous amount of stable solutions, but would be unable to determine whether the ground state has been found. We therefore consider the simplest possible cubic arrangement: That of eight dipoles. The resulting upper bound for the number of equilibrium solutions, $S_{\mathrm{max}} = 16\,777\,216$, is still very frightening. Fortunately, Schönke *et al.* (2015) showed that many of these solutions are equivalent to each other because of symmetry arguments. They were able to calculate the complete set of zero-dimensional solutions, yielding a number of 1 594 032 in total. Of these, 9536 solutions are real and thus physically meaningful. They can be boiled down further to only 183 families of equivalent discrete equilibrium solutions. Furthermore, they found that four one-dimensional solutions exist, of which one constitutes the ground state of the system. With this continuum solution, we not only get a description of the energetic ground state of the cube, but are presented with an unique feature: The orientation for each dipole in this state is infinitely geometrically frustrated. While every dipole is aligned perpendicular to the respective space diagonal of the cube, it can be turned freely into any direction within this plane, provided that the other seven follow accordingly. An exemplary depiction of such a ground state with the respective sense of rotation for each dipole can be found in Fig. 3 of publication 3. Furthermore, minor deviations from the dipole positions are expected to change the energy of the ground state only in a linear way, as the stability analysis in the supplementary information of the work of Schönke *et al.* (2015) shows. That is, the ground state properties appear to be fairly robust. Therefore, an experimental realization of such a cogging-free clutch is feasible.

To approach this, we drastically scale this problem up beyond the nanoscale under the use of a proper permanent magnet material to macroscopic spheres. In the 1980s, an alloy of neodymium, iron, and bor has been discovered to yield the strongest permanent magnets there are to this date (Croat *et al.*, 1984; Sagawa *et al.*, 1984). By now, these magnets are fairly easy to manufacture and widely commercial available. While they can be purchased in high quantities as toys to build appealing structures out of balls with diameters as little as three millimeters, these spheres are distributed by the same manufacturers up to four centimeters in diameter. Spheres of this size that are in direct contact with each other and aligned vertically are reported to hold a mass of 23 kg against gravity (Webcraft GmbH, 2021). From a scientific point of view, permanent magnetic spheres are remarkable since their outer magnetic field resembles that of a point dipole located at the center of the sphere.

For our experiments, we choose a set of spheres with 19 mm diameter which were also used in experiments by Schönke *et al.* (2016). While they already exhibit a strong magnetic field of about one Tesla on the surface, they are still fairly easy to safely deal with.

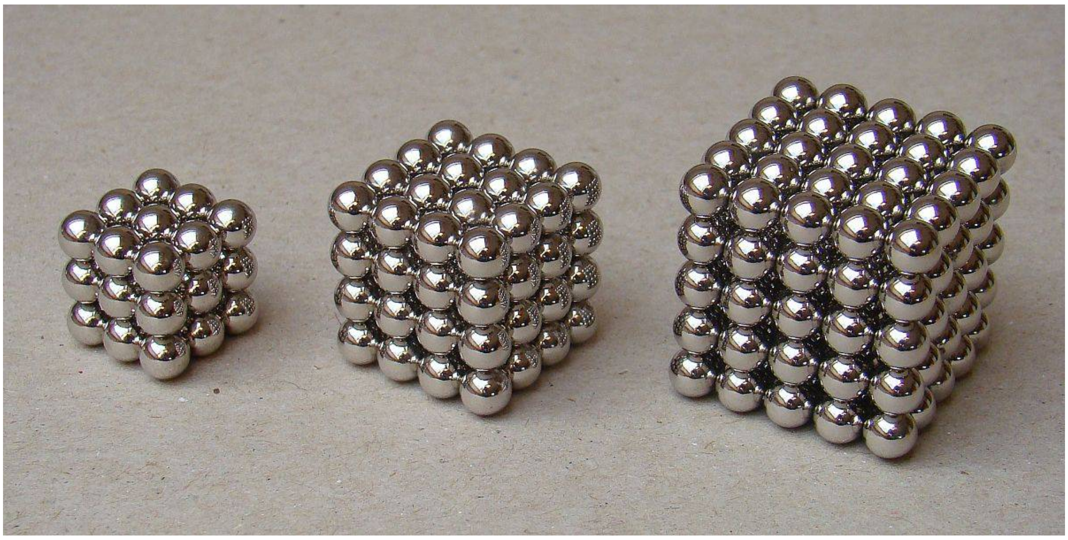

Figure 3.1: Cubes assembled from spherical permanent magnets (Zawischa, 2021).

With macroscopic spheres, one can build simple cubic lattices of different size (see Fig. 3.1). Even though their assembly is remarkably challenging for some edge lengths, all of them are stable in their cubic arrangement. For edge lengths of three, four and five balls, the corresponding experimental realization is shown in Fig. 3.1.

However, within these final lattices, a twist of arbitrary magnets in such a way that their dipole moment is turned out of its original orientation generally leads to an unwanted deconstruction of the whole cube. With one exception: The $2 \times 2 \times 2$ cube. After its assembly, we are able to freely turn each magnet relative to the respective space diagonal, given that the remaining seven magnets have freedom of movement – they turn as well, displaying a seven-fold coupling (see the right-hand side of Fig. 1 of the supplementary information of (Schönke *et al.*, 2015)).

The magnetic field of this arrangement has been measured extensively as described in publication 3. The far field of this arrangement decays like $\frac{1}{r^7}$, which is a characteristic feature of a dotriacontapole. From the center of the cuboid, it increases with the fourth power of the distance. Beyond that, it has been experimentally established that the external magnetic field of a neodymium sphere does indeed follow that of a point dipole with a precision of better than one percent.

4 Special Features of Permanent Magnet Couplings

While the cuboid led to the finding of a seven-fold magnetic clutch, a technical application of this arrangement has not yet been developed. Of practical interest are magnetic clutches formed by two dipoles, one rotated by a motor, the other driven by the magnetic coupling. The milk frother might be the most prominent example. This arrangement becomes amazingly complicated when the two axes of the driving and the driven dipole are not collinear. The most fascinating result is that two cogging-free arrangements can be found here, with different sense of rotation (Borgers *et al.*, 2018). The dynamic behavior of this arrangement has been experimentally explored in publication 4.

A mathematical model for the dynamics of the output shaft is proposed, which includes two types of friction in the bearing. This simplified model describes the experimental findings on a semi-quantitative level. In particular, it can reproduce T periodicity, T/2 periodicity, and chaotic responses. Moreover, it helps to understand the nature of the bifurcations between these different states. Most importantly, it clarifies the parameter range for a safe operation of this magnetic gear: The driving frequency needs to be sufficiently low, and the shaft angle, which quantifies the amount parallel shift of the axes, needs to be sufficiently far from $\Theta = 35.26°$, the angle where the output rotation changes its sign.

Outlook

Figure 10 in publication 4 demonstrates the possibility of bistable behaviour involving a locked and a slip-through state only theoretically. Experimental measurements of that behavior were not presented in that publication. Those measurements were performed later and are presented for the first time in Fig. 4.1 below.

To demonstrate the bi-stable state within the driving frequency range of the setup, the geometrical configuration of the apparatus had to be changed. The distance between the two magnets was increased to $r = 100\,\mathrm{mm}$ to weaken the magnetic interaction. The experimental results obtained in the driving frequency range between 1.00 Hz and 1.25 Hz are shown in Fig. 4.1 both for a clockwise (cw) and counter clockwise (ccw) operation of the drive. For sufficiently slow driving frequencies, the locked state is achieved. It is characterized by exactly one rotation of the output within one driving cycle. For higher frequencies, the output might slip though. It still rotates in this state, but the number of output rotations per driving cycle is smaller than 1. For a driving frequency of 1.2 Hz, 0.0394 is found, which corresponds to one rotation of the output within 25.4 rotations of the driving input. Note that different numbers were obtained for clockwise and counter clockwise operation. This feature cannot be explained on the basis of the theoretical model provided in publication 4. The handedness of these results is an artifact of some broken symmetry in the experimental setup, which is not yet detected unambiguously.

The rotations of the output can be compared with the theoretical expectation based on the numerical integration of eq. (22) from publication 4. The parameters for the friction and magnetic interaction needed to be remeasured for this new experimental setup. They are $\zeta = 0.804$, $\eta = 13.297$ and $g_\tau = 5.784^2$. The values obtained for the counter clockwise rotation seem to be in reasonable agreement with the numerical data. The range of the locked state is larger in the experiment, however. This might be caused by the distortion involved in changing the frequency experimentally, which is presumably larger than the distortion in the numerical procedure. From a technical point of view, the fact that the locked state seems to have a larger basis of attraction than the slip through state can be considered as an advantage, because in most applications one would be interested to operate the gear in the locked state.

While for the slipping state published in Fig. 10 of publication 4 no a priori knowledge of the number of rotations per driving cycle is available, any real number seems possible here. The situation is different for any $\Delta \neq 0$ (In Fig. 4.1, $\Delta = 9°$ was used). Here, it seems more natural to expect periodic solutions of the output, where the period is an integer multiple of the driving period. If such a period could be detected in the numerical integration, it is plotted in Fig. 4.1, together with the corresponding winding number of the output. Most prominent in this figure is the period 3 state with a winding number of 1, e. g., the input needs 3 rotations to turn the output only once.

The most exotic combination in this plot is one with a periodicity of 17 and a winding number of 4. The frequency range for the existence of this state is comparably small, as indicated by the zoom provided in Fig. 4.2. It shows that it is only present within a driving frequency range of 40 mHz. The inset shows the trajectory of this attractor in the α-β plane, similar to the insets of Figs. 9 and 10 of publication 4. The inset on the right hand side provides the same information on the surface of a torus.

Additional aspects of the situation shown in Fig. 4.2 can be found in the screenshot of an interactive analysis program shown in Fig. 4.3. In the Poincaré map Fig. 4.3(g) and the return map Fig. 4.3(h), the 17 revolutions are visible which the output must undergo until it reaches its first repetition. While it is easy to confirm a periodic response with these tools once the output reaches its first repetition, it is difficult to make a definitive assumption beforehand. In Fig. 4.4 the scenario for a yet undefined state is shown. Here, no repetition is found after the depicted 170 rotations of the input. For the simulated data of Fig. 4.1, the period length is determined with the help of Fig. 4.3(h) by counting the number of points in that plot. Points are considered as equal if their distance is smaller than a certain value. For high period lengths this method is not sufficient. Therefore, further work would be necessary to differentiate between high period lengths and a non-periodic response.

Higher numbers of periodicity larger than 17 are presumably also possible, but have not been investigated in detail yet. The detection of those states is time consuming, and the experimental data did not provide a motivation to dig deeper here, because they did not show any of these higher periods. This is presumably due to

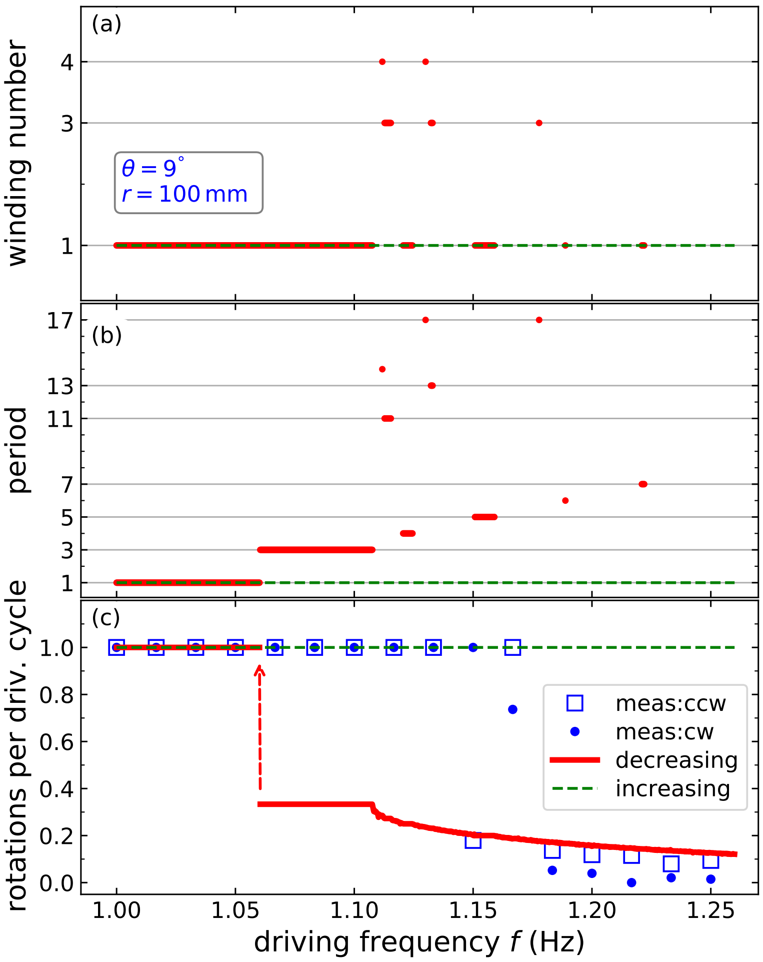

Figure 4.1: Experimental and numerical data from the locked and the slip through state for different driving frequencies. Blue dots correspond to clockwise and blue squares to counter-clockwise rotation of the input in the experiments that were started from the steady state. Red dots show the numerical results for decreasing, the green dashed line for increasing steps of the driving frequency, starting at the highest value and ending there again. The red arrow marks the end of the slip through state in the decreasing branch.

relatively large steps of frequency resolution, and the limited amount of stability of our experimental parameters.

In Fig. 7 of publication 4, we showed that with parallel shaft angles of $\Theta = 35.26°$, we reach the point where the output rotation changes its sign and experience a chaotic response in this area. The underlying mechanism is now analyzed in detail in Fig. 4.5. Here, the output rotations per driving cycle average out to zero at $\Theta = 35°$ and $\Theta = 37.5°$. Another important result is the occurrence of period doubling of

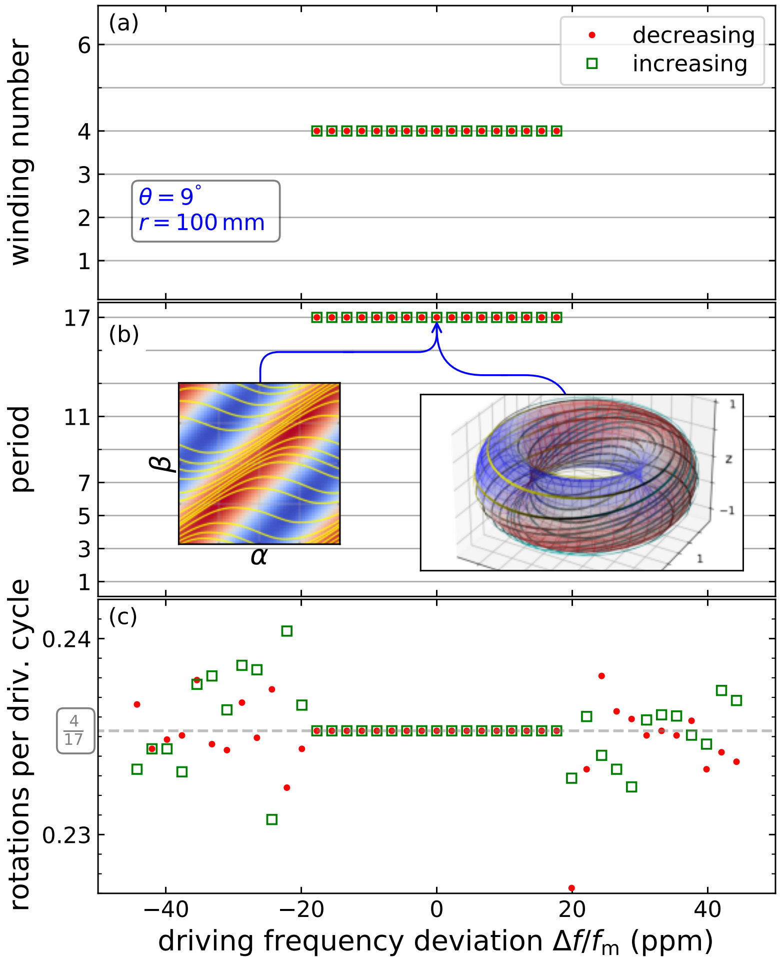

Figure 4.2: Numerical data showing a commensurable relation between period and winding number in the slip through state around the driving frequency of 1.13 Hz. The green empty squares depict increasing, the red circles decreasing frequency steps. The left inset shows the phase trajectory (yellow line) modulo 360°. Red areas denote high, blue areas low potential energy. The right inset shows this trajectory on the surface of a torus. A revolution with the major radius corresponds to a full input rotation, a revolution with the minor radius to a full output rotation. Trajectories are shown in the complementary color of the underlying surface.

the output response relative to driving period at $\Theta = 32.5°$. The period becomes immeasurable with our numerical method at $\Theta = 35°$. It remains to be investigated whether a period doubling cascade leading into a chaotic response occurs here.

The geometric arrangement is undoubtedly a key factor determining the sense of the output rotation in our magnetic coupling. Nevertheless, our numerical results show that it is not the only one: The sense of rotation can also be changed by

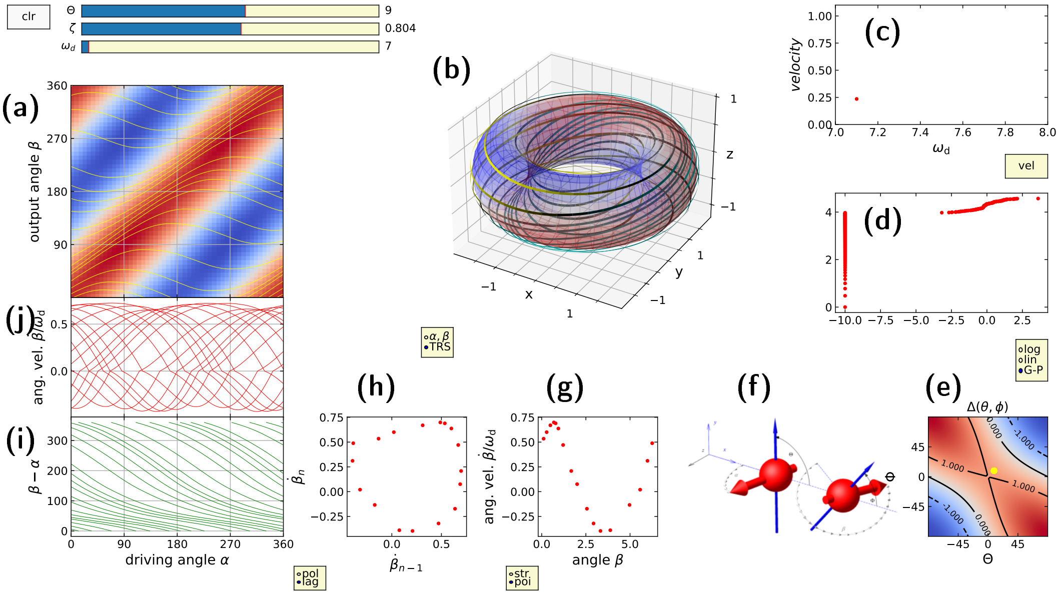
clr
Θ
9
ζ
0.804
ω_d
7
(a)
output angle β
360
270
180
90
(b)
x
y
z
α, β
TRS
(c)
velocity
ω_d
vel
(d)
log
lin
G-P
(e)
Δ(θ, φ)
Θ
(f)
(g)
ang. vel. β̇/ω_d
angle β
str
poi
(h)
β̇_n
β̇_{n−1}
pol
lag
(i)
β − α
driving angle α
(j)
ang. vel. β̇/ω_d

Figure 4.3: Screen shot from an interactive simulation. 170 consecutive driving cycles are shown at a an angular driving frequency of $\omega_\mathrm{d} = 7\,\mathrm{s}^{-1}$. (a) shows the trajectory of $\beta(\alpha)$ modulo 360° as a yellow line. The background shows the areas of high (low) potential energy in red (blue). In (b) the trajectory is shown on a torus. The surface has the same color coding as in (a), the trajectory has the respective complementary color. (c) shows the normalized velocity $\dot\beta/\dot\alpha$ updated after each turn of the input as a function of the respective ω_d. In (d) the distances between points in the return map (h) are shown on the x-axis, with the logarithmic frequency of their occurance on the y-axis. The shaft orientation index Δ is shown in (e) for the shaft angles Θ and Φ, high values in red, low in blue. The yellow circle shows the current system geometry, which is illustrated in (f). (g) shows a Poincaré map of the system. In (i) the angle difference between input and output is shown in relation to the input angle. The angular velocity of the output is shown in (j).

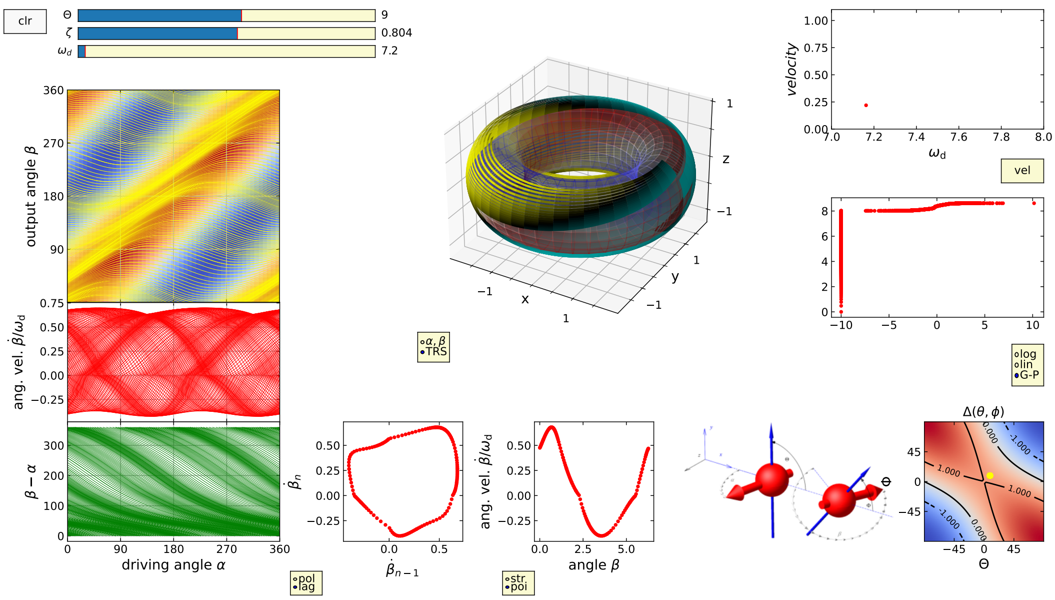

Figure 4.4: Screen shot from the interactive simulation, explained in Fig 4.3. 170 consecutive driving cycles are shown at a an angular driving frequency of $\omega_\mathrm{d} = 7.2\,\mathrm{s}^{-1}$.

slightly tuning the absolute value of the driving frequency. For a constant shaft angle of $\Theta = 31°$, the data is shown in Fig. 4.6. For driving frequencies f smaller than 0.75 Hz, the output follows the input in the same rotation sense. For frequencies between 0.8 Hz and 1.05 Hz the coupling undergoes a slip through motion similar to that in Fig. 4.1, in which the input must undergo three revolutions for one output rotation. If the frequency is further increased to 1.1 Hz, the input still slips through, but now the sign of the output rotation changes. A depiction of the respective trajectories of these phases is found in the insets in Fig. 4.6 (b). In the range from 1.15 Hz to 1.40 Hz, the locked state with the initial sense of rotation is recovered. A driving frequency of 1.40 Hz is necessary to fall into the slip through state again. In this phase the rotations per driving cycle roughly decrease with increasing f and a hysteresis is present between the response for increasing and decreasing frequency steps. Beyond a driving frequency of 1.9 Hz, the output rotation is fully opposed to that of the input, resulting in a locked state with opposite rotation sense of the two magnets.

The frequency tuning of our setup is currently too coarse to reproduce this effect experimentally. In a future work, an upgrade of the driving motor would be necessary. In addition, a transition towards air bearings could help to further reduce the noise in our system to obtain reproducible results.

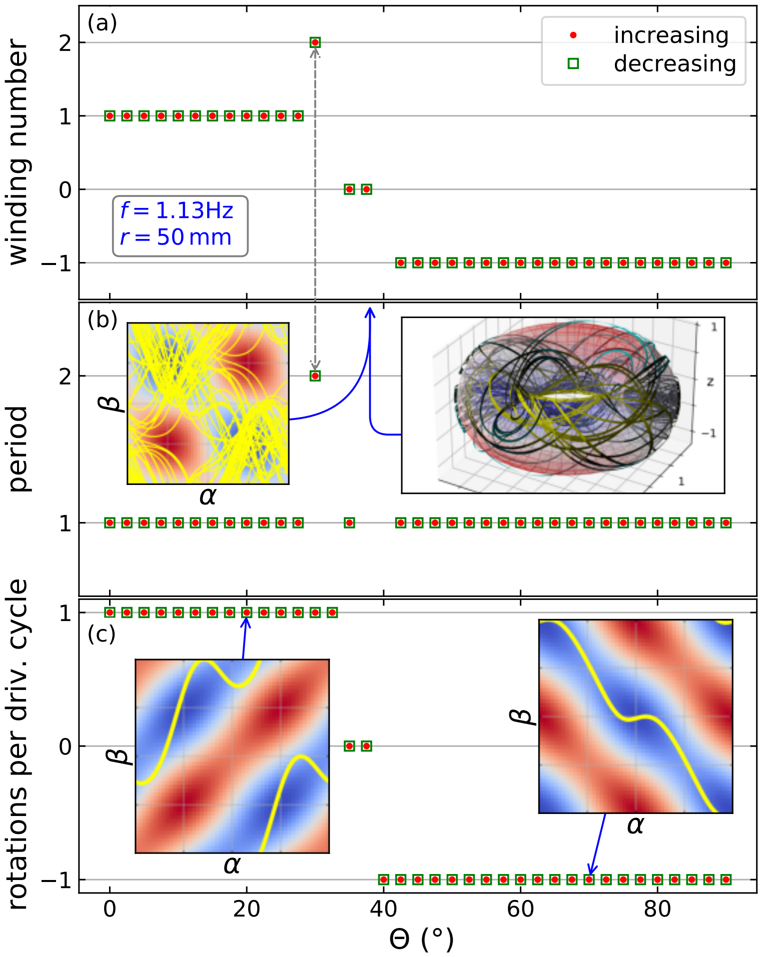

Figure 4.5: Theoretical characterization of the output movement for different shaft angles Θ. Red dots mark increasing, green squares decreasing steps in angular shift. In (c) the rotations of the output per driving cycle of the input are shown. The left inset shows the trajectory for $\Theta = 20°$, the right inset for $\Theta = 70°$. In (b) the input period for periodic solutions is shown. The insets show the energy landscape and trajectory for $\Theta = 37.5°$ and 50 driving cycles. In (a) the winding number of periodic solutions is shown. For clarity, the grey arrow connects the winding number at $\Theta = 30°$ with the corresponding period.

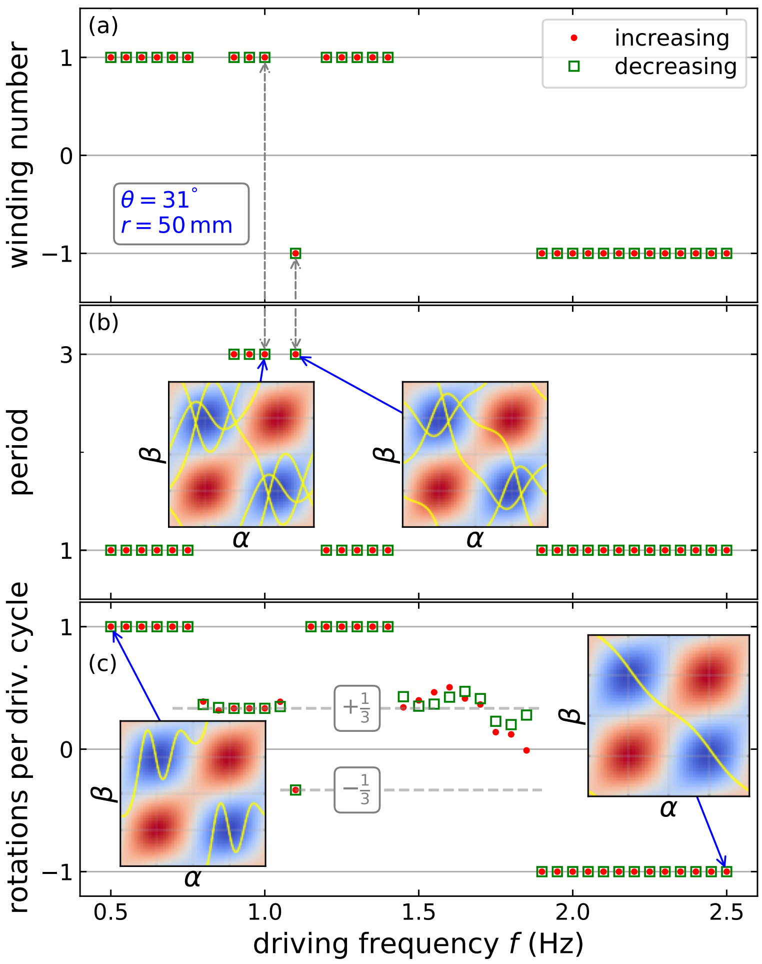

Figure 4.6: Characterization of the output movement for different driving frequencies f. The y-axes and color code are the same as in Fig. 4.5. The left inset in (b) shows the trajectory for 1.0 Hz, the right one for 1.1 Hz. The grey arrows connect their corresponding winding numbers and periods. Their representations in (c) are marked with labels and dashed lines. The insets in (c) show the trajectories for 0.5 Hz and 2.5 Hz.

Bibliography

Alphandéry, E. (2014) *Applications of magnetosomes synthesized by magnetotactic bacteria in medicine*. Frontiers in bioengineering and biotechnology **2**, 5.

Araujo, A. C. V., Abreu, F., Silva, K. T., Bazylinski, D. A. & Lins, U. (2015) *Magnetotactic bacteria as potential sources of bioproducts*. Marine drugs **13** (1), 389–430.

Bergmann, L., Raith, W. & Schaefer, C. (2006) *Elektromagnetismus*, *Lehrbuch der Experimentalphysik*, vol. 2. De Gruyter.

Bhishagratna, K. (2006) *The Sushruta Samhita: An English Translation Based on Original Texts*. Chowkhamba Sanskrit series Office, India **1**, 1–2000.

Borgers, S., Völkel, S., Schöpf, W. & Rehberg, I. (2018) *Exploring cogging free magnetic gears*. American Journal of Physics **86** (6), 460–469.

Carus, T. L. (2019) *De rerum natura*. De Gruyter.

Croat, J. J., Herbst, J. F., Lee, R. W. & Pinkerton, F. E. (1984) *High-energy product Nd-Fe-B permanent magnets*. Applied Physics Letters **44** (1), 148–149.

Ivanov, A. O., Kantorovich, S. S., Reznikov, E. N., Holm, C., Pshenichnikov, A. F., Lebedev, A. V., Chremos, A. & Camp, P. J. (2007) *Magnetic properties of polydisperse ferrofluids: A critical comparison between experiment, theory, and computer simulation*. Physical Review E **75** (6), 061405.

Jacob, J. J. & Suthindhiran, K. (2016) *Magnetotactic bacteria and magnetosomes – Scope and challenges*. Materials Science and Engineering: C **68**, 919–928.

Mickoleit, F., Altintoprak, K., Wenz, N. L., Richter, R., Wege, C. & Schüler, D. (2018) *Precise assembly of genetically functionalized magnetosomes and tobacco mosaic virus particles generates a magnetic biocomposite*. ACS applied materials & interfaces **10** (44), 37898–37910.

Needham, J. *et al.* (1976) *Science and Civilisation in China. Vol. 4: Physics and Physical Technology. Part III: Civil Engineering and Nautics*. Orientalische Literaturzeitung **71** (1), 89–93.

Rosensweig, R. E. (2013) *Ferrohydrodynamics*. Courier Corporation.

Sagawa, M., Fujimura, S., Togawa, N., Yamamoto, H. & Matsuura, Y. (1984) *New material for permanent magnets on a base of Nd and Fe*. Journal of Applied Physics **55** (6), 2083–2087.

Schönke, J., Schneider, T. M. & Rehberg, I. (2015) *Infinite geometric frustration in a cubic dipole cluster*. Physical Review B **91** (2), 020410.

Schönke, J., Schöpf, W. & Rehberg, I. (2016) *Magnetkugeln-ein 10-Euro-Labor*. Physik-Journal **15** (4), 31–37.

Stephen, P. S. (1965) *Low viscosity magnetic fluid obtained by the colloidal suspension of magnetic particles*. US Patent 3,215,572.

Taheri, S. M., Michaelis, M., Friedrich, T., Förster, B., Drechsler, M., Römer, F. M., Bösecke, P., Narayanan, T., Weber, B., Rehberg, I. *et al.* (2015) *Self-assembly of smallest magnetic particles*. Proceedings of the National Academy of Sciences **112** (47), 14484–14489.

Webcraft GmbH (2021) *Kugelmagnet 40 mm, verchromt - supermagnete.de*. `http://www.supermagnete.de/magnetkugeln-neodym/kugelmagnet-40mm_K-40-C`. Accessed: 2021-04-14.

Yan, L., Zhang, S., Chen, P., Liu, H., Yin, H. & Li, H. (2012) *Magnetotactic bacteria, magnetosomes and their application*. Microbiological research **167** (9), 507–519.

Zawischa, D. (2021) *Das Neodym-Magnetkugel-Puzzle*. `https://www.farbeinf.de/magnetkugeln.html`. Accessed: 2021-04-14.

List of Publications

Peer-reviewed Publications

- Hartung, S., Sommer, F., Völkel, S., Schönke, J. & Rehberg, I. *Assembly of eight spherical magnets into a dotriacontapole configuration.* Physical Review B, 98, 214424 (2018).
- Rehberg, I., Richter, R., Hartung, S., Lucht, N., Hankiewicz, B. & Friedrich, T. *Measuring magnetic moments of polydisperse ferrofluids utilizing the inverse Langevin function.* Physical Review B, 100(13), 134425 (2019).
- Rehberg, I., Richter, R. & Hartung, S. *Graphical Magnetogranulometry of EMG909.* Journal of Magnetism and Magnetic Materials, 166868 (2020).
- Hartung, S. & Rehberg, I. *Dynamics of a magnetic gear with two cogging-free operation modes.* Archive of Applied Mechanics, 1-13 (2020).

Posters and Oral Presentations

- Hartung, S., Rehberg, I. & Richter, R. *The magnetic snail.* 14th German Ferrofluid Workshop, Ilmenau (2014).
- Hartung, S., Kador L., Schedl, A., Kreger K. & Schmidt, H.-W. *Large-Area Surface Relief Gratings on Thin Films of Azobenzene-Containing Molecular Glasses.* DPG Conference on condensed matter, Dresden (2017).
- Borgers, S., Völkel, S., Hartung, S., & Rehberg, I. *Cogging free magnetic gears.* DPG Conference on condensed matter, Berlin (2018).
- Hartung, S., Sommer, F., Völkel, S. & Rehberg, I. *Dotriacontapoles – strange magnetic clusters.* 3rd Ilmenau Symposium on Medical Application of Magnetic Nanoparticles and Ferrofluids (ISMAP), Ilmenau (2019).
- Rehberg I., Richter R., Hartung, S. & Friedrich, T. *Rectifying Magnetization Curves.* International Conference on Magnetic Fluids, Paris (2019).
- Hartung, S., Völkel, S. & Rehberg, I. *Dynamics of magnetic gears.* DPG Conference on condensed matter, Regensburg (2019).
- Rehberg, I., Richter, R., Hartung, S., *Graphical Magnetogranulometry.* 79th International Scientific Conference of the University of Latvia, Latvia (2021).

- Rehberg, I., Richter, R., Hartung, S., *Graphical Magnetogranulometry.* Virtual DPG Conference on condensed matter (2021).
- Hartung, S., and Rehberg, I. *Overload dynamics of a magnetic gear with two cogging-free operation modes.* Dynamics Days, Nice (2021).

Part II

Publications

Publication 1

Measuring magnetic moments of polydisperse ferroluids utilizing the inverse Langevin function

Ingo Rehberg, Reinhard Richter, Stefan Hartung, Niklas Lucht, Birgit Hankiewicz, and Thomas Friedrich

Physical Review B, 100, 134425 (2019)
(DOI: 10.1103/PhysRevB.100.134425)

Reprinted with permission.
©2019 American Physical Society

Ingo Rehberg contributed (40 %) the idea and concept for the graphical rectification method, the code for its implementation, the creation of figures 1 and 3 and the manuscript.

Reinhard Richter contributed (20 %) the design and execution of all experiments for measuring the magnetization curves.

My contribution (25 %) consists in analysing the data and creating figures 2,4 and 5.

Niklas Lucht contributed (5 %) the synthetis of the ferrofluid.

Birgit Hankiewicz contributed (5 %) the supervision of the ferrofluid synthesis.

Thomas Friedrich contributed (5 %) to the design of the sample holder.

PHYSICAL REVIEW B **100**, 134425 (2019)

Measuring magnetic moments of polydisperse ferrofluids utilizing the inverse Langevin function

Ingo Rehberg,[1] Reinhard Richter,[1] Stefan Hartung,[1] Niklas Lucht,[2] Birgit Hankiewicz,[2] and Thomas Friedrich[3]

[1]*Experimental Physics 5, University of Bayreuth, 95440 Bayreuth, Germany*
[2]*Institute of Physical Chemistry, University of Hamburg, 20146 Hamburg, Germany*
[3]*Institute of Medical Engineering, University of Lübeck, 23562 Lübeck, Germany*

(Received 24 July 2019; published 18 October 2019)

The dipole strength of magnetic particles in a suspension is obtained by a graphical rectification of the magnetization curves based on the inverse Langevin function. The method yields the arithmetic and the harmonic mean of the particle distribution. It has an advantage compared to the fitting of magnetization curves to some appropriate mathematical model: It does not rely on assuming a particular distribution function of the particles.

DOI: 10.1103/PhysRevB.100.134425

I. INTRODUCTION

Ferrofluids, i.e., colloidal suspensions of magnetic particles, can be characterized by their magnetization curve, which reveals superparamagnetic behavior [1]. In particular, it is possible to obtain an estimate of the dipole moment distribution of the colloidal particles within the fluid from that curve [2], which provides a convenient kind of magnetogranulometry [3]. Knowledge of the size distribution is of importance to understand the dynamic behavior of ferrofluids [4]. The underlying analysis of the magnetization curves is well defined for the case of small particle concentrations, where the interaction of the individual magnetic particles can be neglected. The examination of the magnetization curves is thus a suitable tool to get an idea about the particle size distribution within the fluid, and in particular, it is suitable to resolve changes of the distribution, i.e., to monitor and characterize the aging of a colloidal suspension of magnetic particles. The extraction of the moment distribution function is done by assuming some continuous distribution function like, e.g., the gamma- or log-normal distribution with adjustable parameters. The distribution function is then obtained by fitting the corresponding magnetization curve to the measured one. Some examples, together with a critical comparison, are presented in Ref. [5]. Alternatively, a distribution with discrete δ peaks can be assumed [6,7]. If no knowledge about the particle distribution function is available, an unprejudiced ansatz can be made in connection with a regularization scheme. This procedure yields at least reproducible results for the particle distribution function, an example is given in Ref. [8]. If the resulting distribution functions contain negative concentrations, additional mathematical insights are needed in order to interpret the results.

In the dilute limit, the computed magnetization curve is a folding of the Langevin function—which describes the magnetization of a sufficiently dilute monodisperse solution—with the assumed particle size distribution function. For this kind of extraction procedure, the Langevin function has an unpleasant feature: The folding of different distribution curves with that function can give very similar, almost identical, results [9]. The situation is comparable to the method of extracting the characteristics of a polydisperse particle size distribution from the analysis of dynamic light scattering experiments, a prominent example for a mathematically ill-conditioned problem [10]. The corresponding aspect of the Langevin function has been discussed in some detail by Potton *et al.* [11], who used a maximum entropy method to face the ensuing complications.

In this paper we demonstrate a method which circumvents these difficulties by not even trying to obtain the complete distribution function. It is basically a graphical rectification of the magnetization curve and reveals important parameters of the magnetic moment distribution, but does not rely on assuming a particular distribution function of the magnetic particles. Our analysis of the rectified curves is, however, based on the limit of small concentrations. For larger concentrations, the interaction between the magnetic particles lead to additional complications [5,12] which are not addressed in the present paper.

To give a motivation for the method, Fig. 1 provides an example of this rectification method to characterize an aging process of a ferrofluid. It makes use of data taken from the literature [6,7] describing the formation of magnetic clusters in a colloidal suspension of nanocubes. They characterize the aging of cubic nanoparticles (8 wt %, iron oxide, edge length 9 nm) in solution triggered by a magnetic field (800 kA/m for 4 h). Figure 1(a) shows magnetization curves of that fluid for three different times. They were obtained with a vibrating sample magnetometer described in detail by Friedrich *et al.* [13]. The first data set was obtained for a relatively fresh sample, which had been exposed to a magnetizing field of about 800 kA/m for 4 h. The magnetization curves in Fig. 1(a) show an increasing slope with the time elapsed. This aging process is interpreted as the manifestation of the clustering of the magnetic particles. Some features of the change of these curves can be seen more clearly in Fig. 1(b). Here the appropriately scaled slope of the inverse Langevin function L^{-1} of the magnetization data has been plotted. The ensuing curves yield the arithmetic mean of the dipole distribution at its center, and the harmonic mean as the asymptotic value for large polarizing fields.

©2019 American Physical Society

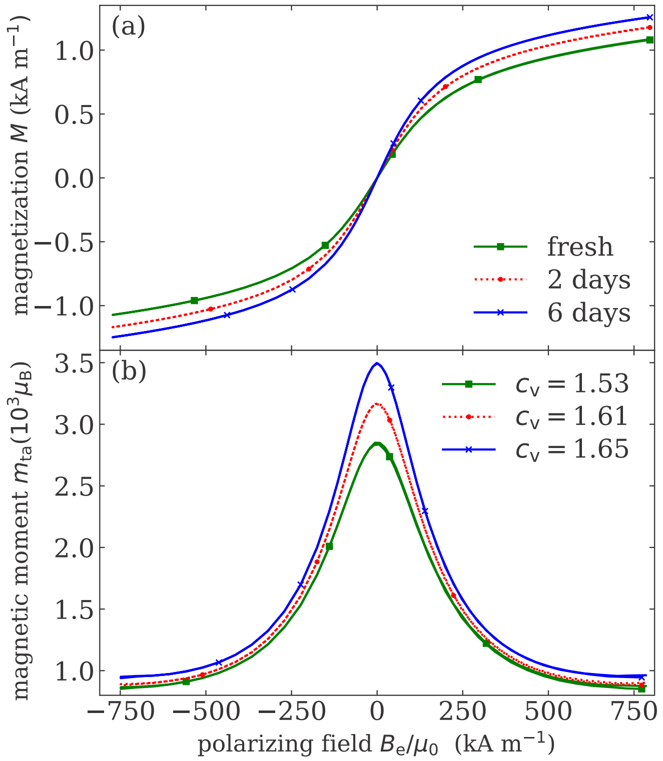

FIG. 1. Aging of a nanocube fluid. (a) The magnetization of a freshly prepared ferrofluid is presented together with one obtained two (six) days later. During the measurements, the magnetizing field strength went from about 750 to −750 kA/m and back within a period of 108 min. The measurements are presented as polygonal lines, every 30th data point is shown to label them. (b) The curves shown in the lower part are derived from the magnetization curves and give information about the magnetic moments of the suspended particles. The maximum corresponds to the arithmetic mean m_a, and the asymptotic value for large polarizing fields to the harmonic mean m_h. The corresponding estimator for the coefficient of variation c_v is listed in the lower legend.

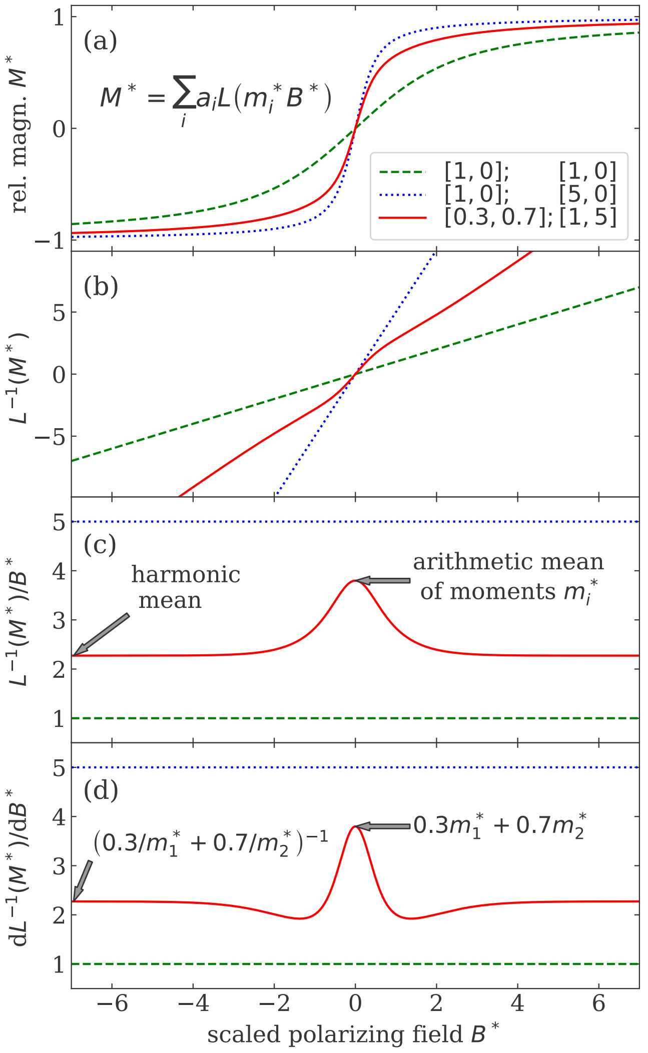

FIG. 2. The data processing demonstrated by three artificial magnetization curves. (a) The magnetization curves of two monodisperse (dashed and dotted lines) and a bidisperse solution. The first pair of numbers in the legend represents the relative fraction a_1 and a_2, and the second one the corresponding magnetic moments m_1 and m_2. (b) The inverse Langevin function L^{-1} of the relative magnetization. The straight dashed and dotted lines correspond to the two monodisperse distributions, the slightly curved solid line to the bidisperse distribution. (c) The chord slope of the rectified curves. The monodisperse distributions lead to constant values (dashed and dotted lines) which represent the strengths of the magnetic dipole moment. The bidisperse curve yields the arithmetic mean of the two contributing moments as its maximum value, and the harmonic mean as the asymptotic value for large polarizing fields. (d) The tangential slope of the $L^{-1}(M^*)$ curves.

II. METHOD

To explain this, we illustrate the data processing by artificial magnetization curves in Fig. 2. A monodisperse dilute solution of particles with a magnetic moment m is expected to be described by a magnetization

$$M = M_s L\left(\frac{mB}{k_B T}\right), \quad \text{with} \quad L(x) = \coth(x) - \frac{1}{x}.$$

In Fig. 2(a) the abbreviations

$$M^* = M/M_s, \quad m^* = m/\mu_B, \quad \text{and} \quad B^* = B\frac{\mu_B}{k_B T}$$

are used. It displays the magnetization of two monodisperse fluids with $m^* = 1$ and $m^* = 5$, respectively, and one for a bidisperse 30%/70% mixture. All three curves show a fairly similar shape. To bring out the difference between these curves more clearly, it helps to take the inverse Langevin function $L^{-1}(M^*)$ as shown in Fig. 2(b). The two monodisperse curves reveal a constant slope—in this sense the magnetization curve is rectified—while that of the mixture appears slightly more complicated. To bring out these differences quantitatively, both the chord slope $m^*_{\rm ch} = \frac{L^{-1}}{B*}$ or the tangential slope $m^*_{\rm ta} = \frac{dL^{-1}}{dB*}$ can be used to obtain a value for what can be called an "effective magnetic moment." $m^*_{\rm ch}$ is shown in Fig. 2(c) and the tangential slope $m^*_{\rm ta}$ in Fig. 2(d). In both cases, the monodisperse curve yields the constant value m^*, which is proportional to the magnetic moment of the particles.

The more interesting part is the interpretation of the nonconstant curves obtained for the bidisperse mixture. Both methods yield the same maximum in the center, i.e., for the magnetizing field $B^* = 0$. Near this point $L(B^*m^*) \approx \frac{B^*m^*}{3}$, thus the derivative represents the appropriately weighted sum of the two slopes of the monodisperse magnetization curves, i.e., the arithmetic mean $m_{\text{a}}^* = \langle m_i^* \rangle$ of the magnetic moments involved. Its value is $0.3m_1 + 0.7m_2 = 3.8$ for this particular example.

Both methods also yield the same results for large values of B^*. For the interpretation of this value, one has to recall that the Langevin function converges to its asymptotic value 1, like $1/(B^*m^*)$, which means that the slope is inversely proportional to the magnetic moment. Consequently, the slope for the bidisperse curve can be obtained by the weighted sum of the inverse moments, the harmonic mean $m_{\text{h}}^* = \langle 1/m_i^* \rangle^{-1}$. It is $(0.3/m_1 + 0.7/m_2)^{-1} \approx 2.27$ for this example.

Whether the chord slope or the tangential slope should be used to obtain the effective magnetic moment for real data is a practical issue. When dealing with a poor signal/noise ratio, data obtained from the chord slope have the advantage to show less scatter. On the other hand, the effective magnetic moments obtained from the tangential slope have the advantage to converge faster towards the asymptotic limit, which is important when the scaled applied field B^* is still far from the saturation field. A practical value for judging the strength of the polarizing field could be given by that field where the magnetization reaches 90% of M_{s}. The value for the corresponding polarizing field is then given by $L(m^*B^*) = 0.9$, yielding $B^* = L^{-1}(0.9)/m^* \approx 10.0/m^*$.

The difference between the arithmetic and the harmonic mean values, $m_{\text{a}} - m_{\text{h}}$, can be taken as a direct order parameter for the amount of polydispersity: It is zero for a monodisperse distribution and increases with the width of the distribution. In fact, this difference divided by the harmonic mean provides an estimator for the relative standard deviation (RSD, also called coefficient of variation c_{v}). More precisely, we obtain the coefficient of variation as $c_{\text{v}} = \sqrt{\frac{m_{\text{a}} - m_{\text{h}}}{m_{\text{h}}}}$. Additionally, the square root of their product yields an estimator for the geometric mean $m_{\text{g}} = \sqrt{m_{\text{a}} m_{\text{h}}}$. However, these last two statements are only correct for certain distribution functions of the magnetic moment, including the log-normal distribution, which seems to be the most prominent one assumed within the granulometric analysis of magnetization curves.

To illustrate the procedure with more realistic distributions than the artificial bidisperse one used in Fig. 2, we compare this bidisperse distribution with a suitably chosen log-normal and gamma distribution [5]. More precisely, in both cases we chose that distribution which has the same arithmetic and harmonic mean as the bidisperse one. This is possible because both functions contain two adjustable parameters. The comparison is presented in Fig. 3. The inset of Fig. 3(a) shows the distribution function for the three cases. The continuous functions are the log-normal and gamma distribution, while the bidisperse distribution function is basically zero, except for the two δ peaks. The corresponding cumulative distribution functions for the three examples are shown in the inset of Fig. 3(b).

Note that in spite of the drastically different distribution functions, the corresponding magnetization curves displayed in Fig. 3(a) are almost nondistinguishable. This is an exemplary illustration of the ill-conditioned nature of magnetogranulometry mentioned in the Introduction.

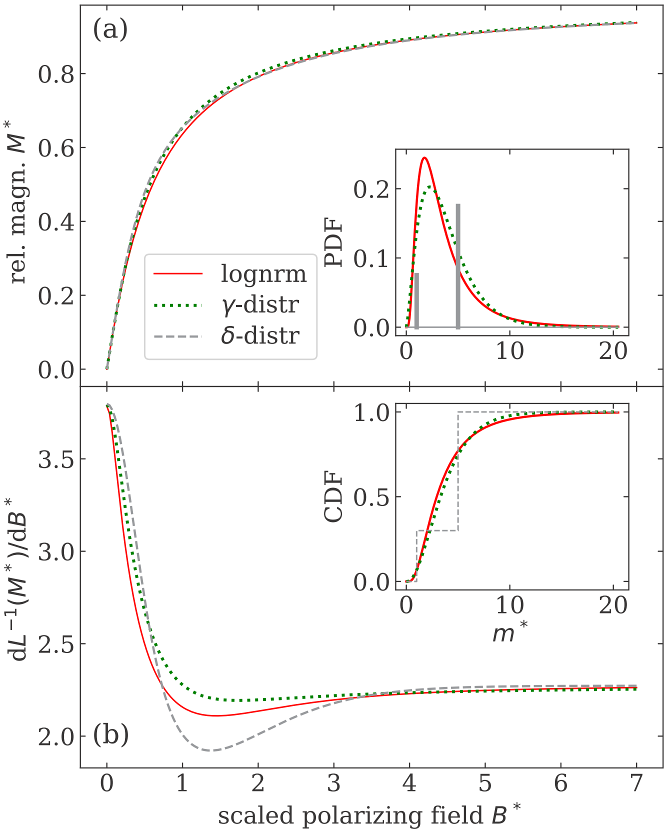

FIG. 3. A comparison between magnetization curves calculated for the bidisperse distribution with two δ peaks introduced in the example in Fig. 2 (dashed gray line), the log-normal distribution (solid red line), and the γ distribution (dotted green line). The parameters are chosen such that all three distributions have the same values of the harmonic and the arithmetic mean. Therefore, all curves in (b) start for $B^* = 0$ at the same value of 3.8 and approach the value of 2.27 for high field strength. The inset (a) shows the partial and inset (b) the cumulative distribution functions of the three distributions.

Taking the derivative of the inverse $dL^{-1}(M^*)/dB^*$ helps to bring out the differences in the three magnetization curves more clearly, as shown in Fig. 3(b). More importantly, this effective magnetic moment m_{ta}^* reveals the correct arithmetic and harmonic mean for all three distribution functions, as expected.

III. EXPERIMENTAL RESULTS

Finally, we would like to illustrate the method by analyzing magnetization curves of two additional samples of ferrofluids. The one measured for commercially available EMG909 (EMG909, Lot H030308A, Ferrotec) is presented in Fig. 4(a). The “polarizing field” used for the horizontal axis is the field acting on a magnetic particle. We used the lowest order to determine that field, namely the Weiss correction $H_{\text{e}} = H_{\text{i}} + M/3$, see, e.g., Ref. [5] for a discussion of this correction. Note that in our case the correction term $M/3$ exactly cancels out the demagnetization factor provided by our spherical sample

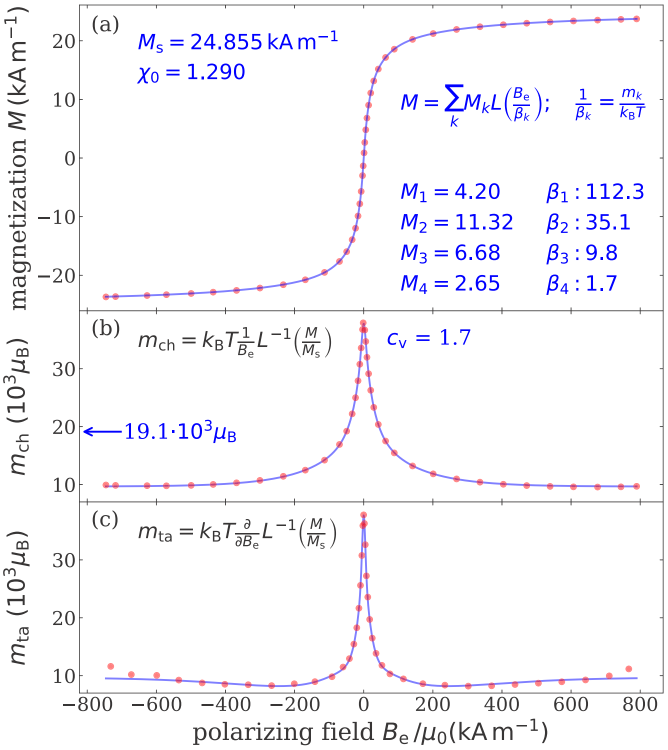

FIG. 4. The method illustrated by the the commercially available ferrofluid EMG909. (a) The measured magnetization curve (red dots, only every 10th data point is shown) is fitted by a superposition of four Langevin functions (solid blue line) indicated by the M_k given in kA m^{-1}. The corresponding β_k yields the magnetic moment m_k provided in kμ_B. The resulting saturation magnetization M_s and the initial susceptibility χ_0 are listed as well. (b) The effective magnetic moment m_{ch} obtained from the data (red dots) and the fitting function (solid blue line). The c_v obtained from the arithmetic and harmonic mean of the magnetic moments is listed, and the blue arrow points to the value of the corresponding geometric mean. (c) The effective magnetic moment m_{ta} obtained from the data (red dots) and the fitting function (solid blue line)

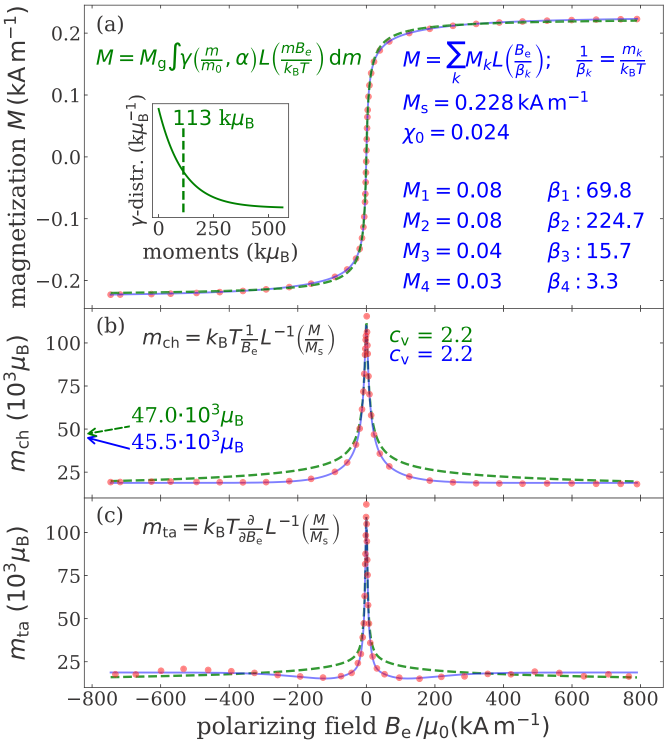

FIG. 5. The method illustrated by a CoFe$_2$O$_4$ ferrofluid. The features are the same as explained in Fig. 4, and in addition, a fit to a γ distribution (solid green line) shown in the inset has been performed here. While the differences of the two fitting functions in (a) are barely visible, (b) and (c) bring out these tiny differences more clearly. The geometric mean of both fits is indicated by the arrows in (b).

holder, leading to $H_e = H_0$, and $B_e = B_0$. Thus, in our case the polarizing field B_e turns out to be the one measured far from our magnetized sphere B_0. Note that the resulting plot—with the effective B_e field used for the x axis—is slightly different from the more common practice, where the inner magnetic field H_i is used for the horizontal axis of the magnetization curve. For the latter kind of plot, however, taking $L^{-1}(M/M_s)$ would not produce a straight line even for a monodisperse ferrofluid. This would make the rectification method proposed here less powerful.

The measured magnetization data can well be represented by a superposition of four Langevin functions

$$M(B_e) = \sum_{k=1}^{4} M_k L\left(\frac{B_e}{\beta_k}\right), \quad \text{with} \quad \frac{1}{\beta_k} = \frac{m_k}{k_B T}.$$

This $M(B_e)$ resulting from this "quad-disperse" distribution function provides a convenient fitting curve for the magnetization data, with the M_k and β_k as fit parameters, and is shown as a solid line in the upper part. It serves primarily for giving a smooth and analytic representation of the data. In addition, it can be used to calculate the so called Langevin susceptibility χ_L as the slope of the magnetization curve in its origin. From χ_L, the initial susceptibility $\chi_0 = \frac{dM}{dH_i}$ is obtained as $\chi_0 = \frac{\chi_L}{1-\chi_L/3}$, which is provided in the figure as well. While this number is an important characteristic number for ferrofluids in general, its value is not needed for the further analysis presented here, but it helps to label the fluid and to judge its concentration. The saturation magnetization can be obtained from the fitting parameters as $M_s = \sum_{k=1}^{4} M_k$.

Figure 4(b) shows the effective magnetic moment m_{ch} obtained from the chord slope. The red dots are obtained directly from the data. The solid blue line stems from the fit to the magnetization curve. Both numbers agree fairly well. Note that there is a small asymmetry with respect to the y axis within the data, which the ansatz for the quad-disperse fitting function cannot produce.

These small differences between the data and the fitted curve can be seen more clearly in Fig. 4(c), where the effective magnetic moment m_{ta} is shown. But even here the signal/noise ratio seems good enough to extract the numbers for m_a and m_h, and the corresponding guesses for the geometric mean m_g and the relative standard deviation c_v.

For demonstrating the method also with a different chemical species, we use a cobalt-ferrite-based ferrofluid. It was synthesized in a one-step process with a subsequent stabilization step after a modified synthesis procedure of Nappini *et al.* [14]. For the synthesis both iron and cobalt salts were precipitated in a boiling solution of sodium hydroxide. The particles were magnetically separated by holding a permanent magnet (with a surface field of about 1 T and a diameter of about 3 cm) onto the reaction vessel for a few minutes and rinsed with water. This step was repeated until a neutral *p*H value was reached, typically about three times, then the particles were stabilized in a sodium citrate solution. The resulting magnetization curve is shown in Fig. 5(a). It can also fairly precisely be fitted by assuming a quad-disperse solution, as shown by the blue line. In addition, we have also fitted a γ distribution here, as advocated in [5]. The resulting distribution is shown in the inset. The corresponding magnetization shown by the green line fits the data almost as good as the quad-disperse one, which is just considered as another manifestation of the ill-posed character of this inverse problem.

Displaying the resulting magnetic moments in Figs. 5(b) and 5(c) brings out the differences between the two magnetization curves more clearly. It also reveals that the quad-disperse fit is closer to the data, which is no surprise, because that fit contains eight fitting parameters, while the γ distribution only has two. With a relative standard deviation of $c_{\mathrm{v}} = 2.2$, the distribution function of the $\mathrm{CoFe_2O_4}$ ferrofluid is wider compared to the EMG909 fluid presented in Fig. 4. That might be a manifestation of the fact that our fluid was relatively freshly prepared, and no special measures were taken in order to obtain a more monodisperse solution. On the other hand, special measures to obtain monodispersity were taken for the fluid analyzed in Fig. 1, which contained originally fairly monodisperse nanocubes. Here the monotonic increase of c_{v} with time is interpreted as a result of the formation of supercubes [6,7].

IV. CONCLUSION AND OUTLOOK

In summary, we have demonstrated the use of a graphical rectification method revealing the characteristic magnetic moments of the particles in a ferrofluid from their magnetization curves. In particular, the arithmetic and the harmonic mean of the moments m_{a} and m_{h} can be read off from a plot of the effective magnetic moment. The method works without the need to assume a specific distribution function, thus circumventing the difficulties stemming from an ill-posed problem for the interpretation of those functions. As secondary results, the method yields a guess for the relative standard deviation c_{v} and the geometric mean m_{g}, although that guess can strictly be justified only for certain distributions including the log-normal one. The method applied here can be justified for dilute solutions, higher order corrections for larger concentrations [5,12] have not been taken into account. A corresponding graphical method for the examination of light scattering data in terms of granulometric information is currently under investigation.

The open source Python code for the graphical display of the magnetization curves together with the ensuing magnetic moments is still under construction, but we are happy to provide the current version on request.

ACKNOWLEDGMENT

It is a pleasure to thank H. R. Brand for stimulating discussions and suggestions.

[1] R. Rosensweig, *Ferrohydrodynamics*, Dover Books on Physics (Dover, New York, 2013).

[2] W. C. Elmore, Phys. Rev. **54**, 1092 (1938).

[3] B. Berkovskiĭ and V. Bashtovoĭ, *Magnetic Fluids and Applications Handbook*, Begell Digital Library (Begell House, Danbury, CT, 1996).

[4] P. Fannin, J. Magn. Magn. Mater. **136**, 49 (1994).

[5] A. O. Ivanov, S. S. Kantorovich, E. N. Reznikov, C. Holm, A. F. Pshenichnikov, A. V. Lebedev, A. Chremos, and P. J. Camp, Phys. Rev. E **75**, 061405 (2007).

[6] S. Mehdizadeh Taheri, M. Michaelis, T. Friedrich, B. Förster, M. Drechsler, F. M. Römer, P. Bösecke, T. Narayanan, B. Weber, I. Rehberg, S. Rosenfeldt, and S. Förster, Proc. Natl. Acad. Sci. U.S.A. **112**, 14484 (2015).

[7] S. Rosenfeldt, S. Förster, T. Friedrich, I. Rehberg, and B. Weber, in *Novel Magnetic Nanostructures*, edited by N. Domracheva, M. Caporali, and E. Rentschler, Advanced Nanomaterials (Elsevier, Amsterdam, 2018), pp. 165–189.

[8] T. Weser and K. Stierstadt, Z. Phys. B: Condens. Matter **59**, 253 (1985).

[9] A. Martinet, in *Aggregation Processes in Solution*, edited by E. Wyn-Jones and J. Gormally, Studies in Physical and Theoretical Chemistry Vol. 26 (Elsevier, Amsterdam, 1983), pp. 509–548.

[10] B. Berne and R. Pecora, *Dynamic Light Scattering: With Applications to Chemistry, Biology, and Physics*, Dover Books on Physics Series (Dover, New York, 2000).

[11] J. A. Potton, G. J. Daniell, and D. Melville, J. Phys. D: Appl. Phys. **17**, 1567 (1984).

[12] J. P. Embs, B. Huke, A. Leschhorn, and M. Lücke, Z. Phys. Chem. **222**, 527 (2009).

[13] T. Friedrich, T. Lang, I. Rehberg, and R. Richter, Rev. Sci. Instrum. **83**, 045106 (2012).

[14] S. Nappini, E. Magnano, F. Bondino, I. P, A. Barla, E. Fantechi, F. Pineider, C. Sangregorio, L. Vaccari, L. Venturelli, and P. Baglioni, J. Phys. Chem. C **119**, 25529 (2015).

Publication 2

Graphical Magnetogranulometry of EMG909

Ingo Rehberg, Reinhard Richter and Stefan Hartung

Journal of Magnetism and Magnetic Materials, 166868 (2020)
(DOI: 10.1016/j.jmmm.2020.166868)

Reprinted with permission.
©2020 Elsevier B.V.

Ingo Rehberg contributed (50 %) the idea and concept for the graphical rectification method, a program for its implementation and the manuscript.

Reinhard Richter contributed (25 %) the design and execution of all experiments.

My contribution (25 %) consists in analyzing the data and presenting the results it in a figure .

Journal of Magnetism and Magnetic Materials 508 (2020) 166868

Contents lists available at ScienceDirect

Journal of Magnetism and Magnetic Materials

journal homepage: www.elsevier.com/locate/jmmm

Graphical Magnetogranulometry of EMG909

Ingo Rehberg[*], Reinhard Richter, Stefan Hartung

Experimentalphysik V, Universität Bayreuth, 95440 Bayreuth, Germany

ARTICLE INFO

Keywords:
Ferrofluid
Magnetogranulometry
Inverse Langevin function
Ferrofluid EMG909 from Ferrotec Co

ABSTRACT

The magnetization curve of the commercially available ferrofluid EMG909 is measured. It can adequately be described by a superposition of four Langevin terms. The effective dipole strength of the magnetic particles in this fluid is subsequently obtained by a graphical rectification of the magnetization curve based on the inverse Langevin function. The method yields the arithmetic and the harmonic mean of the magnetic moment distribution function, and a guess for the geometric mean and the relative standard deviation. It has the advantage that it does not require a prejudiced guess of the distribution function of the poly-disperse suspension of magnetic particles.

1. Introduction

“Die krumme Linie kennt kein größeres Wunder, als die gerade. Aber nicht umgekehrt.” (The bent line does not know a greater marvel than the straight line. But not the other way round.) This statement from Friedrich Hebbel might be easier to justify from an aesthetic than from a mathematical point of view, but can be considered as our guideline in the pursuit of straightening the typical S-shape of magnetization curves to bring out their individual and specific characteristics more clearly. For that purpose, taking the inverse Langevin function of the magnetization seems to be the natural approach [1]. While that rectification effort is expected to work exactly for monodisperse ferrofluids, the outcome for polydisperse fluids is slightly more complicated than just a straight line. However, it turns out to be very useful: It serves to provide the arithmetic and the harmonic mean of the particle distribution function.

In this contribution, we apply that method of “graphical magnetogranulometry” [1] to the magnetization curve of the ferrofluid EMG909, commercially available from Ferrotec Co. This is of special interest within these proceedings, because this fluid had been chosen for the investigation of the magnetically stabilized Kelvin–Helmholtz instability, which was presented at ICMF 2019 [2], and is described in Ref. [3].

2. Magnetization of EMG909

We have measured the magnetization with a vibrating sample magnetometer utilizing a spherical sample holder described in Ref. [4]. The result of this measurement is presented in Fig. 1(a). The ”polarizing field” used for the horizontal axis is the field acting on a magnetic particle. It is determined by the external magnetic field H_0 measured far from the spherical sample, and influenced by the homogeneous magnetization M inside the sphere. We used the lowest order to determine the polarizing field, namely the Weiss correction $H_e = H_i + M/3$, where H_i is the magnetic field inside the spherical sample. A discussion of the Weiss correction and higher order corrections for the effective field H_e can be found in Ref. [5]. For our magnetometer geometry, that correction term $M/3$ exactly cancels out the demagnetization factor provided by the spherical sample holder. This leads to $H_e = H_0$, and correspondingly $B_e = B_0$. Here B_e is the magnetic induction inside the virtual – and hollow – “Weiss sphere”, which is responsible for the torque acting on the individual magnetic particle. In conclusion, in our case and in lowest order approximation the polarizing field B_e turns out to be the one measured far from our magnetized sphere B_0, which is conveniently detected by a Hall probe.

Note that this effective field correction is only a correction to lowest order for reasons of simplicity. According to Eq. (20) of Ref. [5], the next correction term reads $\frac{1}{144}M_L\frac{dM_L}{dH_i}$, which brings only a correction on a sub-percentage scale for the fluid presented here. For fluids with a higher magnetization, that term would become more important, i.e. the estimation of B_e presented here is only a lowest order approximation for sufficiently dilute solutions.

Neglecting this Weiss correction completely would have a measurable effect on the data examination: The initial slope of the magnetization curve would change by about 20% (see Eq. 2 below). This would lead to an error in the estimation of the arithmetic mean of the magnetic moments of the same order of magnitude [1]. The harmonic mean, on the other hand, is determined from the slope of the

---

[*] Corresponding author.
E-mail address: Ingo.Rehberg@uni-bayreuth.de (I. Rehberg).

https://doi.org/10.1016/j.jmmm.2020.166868
Received 30 July 2019; Received in revised form 25 February 2020; Accepted 2 April 2020
Available online 04 April 2020
0304-8853/ © 2020 Elsevier B.V. All rights reserved.

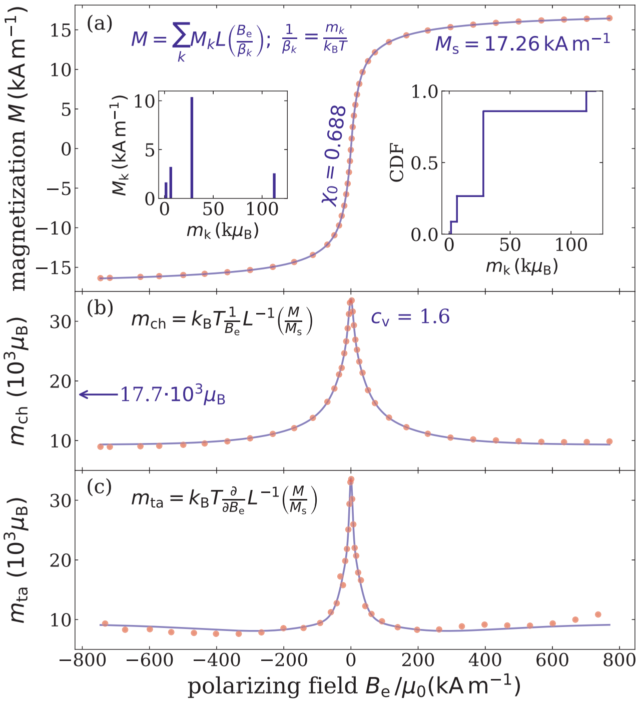

Fig. 1. Examination of the ferrofluid EMG909. (a) The measured magnetization curve (red dots, only every 10th data point is shown) is fitted by the sum of four Langevin terms (solid blue line) indicated by the M_k. The corresponding β_k yields the magnetic moment m_k. The respective M_k and m_k of the fitted function are shown in the left inset, the corresponding cumulative distribution function in the right inset. The resulting saturation magnetization M_s and initial susceptibility χ_0 are listed as well. (b) The effective magnetic moment m_{ch} obtained via the chord slope (Eq. 3) from the data (red dots) and the fitting function (solid blue line). The corresponding c_v (Eq. 4) is listed. The blue arrow points to the value of the corresponding geometric mean (Eq. 5). (c) The effective magnetic moment m_{ta} obtained via the tangential slope (Eq. 6) from the data (red dots) and the fitting function (solid blue line).

magnetization at higher fields where the magnetization is almost saturated and the influence of the Weiss correction term decreases to zero. Thus, the harmonic mean would still be measured correctly, at least asymptotically for large fields. A comparison of the two terms would then lead to a qualitatively wrong statement for a monodisperse fluid: It would be interpreted as a polydisperse one. In conclusion, neglecting the Weiss correction is clearly prohibited for the graphical granulometry [1].

Note that the resulting plot—with the effective B_e-field used for the x-axis—is slightly different from the more common practice, where the inner magnetic field H_i is used for the horizontal axis of the magnetization curve. Our motivation to use B_e instead is the fact that magnetization curves in lowest order can be considered as a superposition of terms

$$\mathrm{L}\left(\frac{B_e m}{k_B T}\right), \text{ or equivalently } \mathrm{L}\left(\frac{\mu_0 H_e m}{k_B T}\right),$$

a fact which is used both for the best-fit curve in Fig. 1(a), and the graphical granulometry provided in Fig. 1(a) and (c).

The magnetization data shown in Fig. 1(a) are obtained as the difference between the magnetization data from the filled and the empty sample holder, which is a lowest order correction for the magnetization of the sample holder. This is only a tiny correction of less than 0.1% for the fairly concentrated magnetic fluid used here, it is nevertheless performed routinely.

It turns out that the measured magnetization data can fairly accurately be represented by a superposition of four Langevin terms

$$M(B_e) = \sum_{k=1}^{4} M_k \mathrm{L}\left(\frac{B_e}{\beta_k}\right), \text{ with } \frac{1}{\beta_k} = \frac{m_k}{k_B T}. \tag{1}$$

This $M(B_e)$ resulting from this "quad-disperse" distribution function provides a convenient fitting curve for the magnetization data, with the M_k and β_k as fit parameters. The result is shown as a solid line in Fig. 1(a). It serves primarily for giving a smooth and analytical representation of the data.

The inset on the left hand side in Fig. 1(a) is a graphical representation of the eight fit parameters. It might serve to give some feeling for the distribution function of the dipole strength in the polydisperse suspension. However, it should not be over-interpreted in this sense, other distribution functions would do the job almost as well, which is due to the ill-posed character of this inverse problem. More illustrations for this point are provided in Ref. [1]. The corresponding cumulative distribution function (CDF) of the quad-disperse distribution is shown in the inset on the right hand side of Fig. 1(a).

Some technical remarks about the fitting procedure have to be made. We found it useful to suppress negative values for the magnetic moments and the magnetization, which is conveniently done by squaring the corresponding terms in the fitting procedure, and finally taking the positive root of the resulting value. The method to obtain the eight fitting parameters of this particular representation contains four steps:

(i) Fit $M(B_e)$ with two parameters M_1 and β_1.
(ii) Keep M_1 and β_1, and allow for two additional fit parameters M_2 and β_2.
(iii) Keep the four parameters, and allow for two additional fit parameters M_3 and β_3.
(iv) Keep the six parameters, and allow for two additional fit parameters M_4 and β_4.

It seems that in principle this list could be extended. In practice, we found for many of the fluids investigated so far that even six parameters are enough to describe the magnetization within the resolution of our data. On the other hand, we never needed more than eight parameters.

For the fitting procedure, we use a standard routine (named curve_fit, from the package scipy.optimze [6]) within the Python program minimizing the deviation between the data and the fitting function. Our program calls this function repeatedly, until a local minimum with respect to all the fit parameters is reached. It seems worth noticing that the ansatz given by Eq. (1) is sufficiently simple and fast, so that the data processing can conveniently be done interactively. The fitting curve provides a noise-free representation of the data. It can be used to calculate the so-called Langevin susceptibility

$$\chi_L = \frac{dM}{dH_e}$$

as the slope of the magnetization curve in its origin. From χ_L, the initial susceptibility is obtained as

$$\chi_0 = \frac{dM}{dH_i} = \frac{\chi_L}{1 - \frac{\chi_L}{3}}, \tag{2}$$

which is provided in Fig. 1(a). This number is an important macroscopic parameter for the hydrodynamic instability of this particular fluid investigated in Ref. [3]. The other important characteristic number is the saturation magnetization of the fluid, which can be obtained from the fitting parameters as

$$M_s = \sum_{k=1}^{4} M_k,$$

a convenient way to extrapolate the data towards $B_e \to \infty$.

Fig. 1(b) shows the effective magnetic moment m_{ch} obtained from the chord slope as

$$m_{\mathrm{ch}} = k_{\mathrm{B}} T \frac{1}{B_{\mathrm{e}}} \mathrm{L}^{-1}\left(\frac{M}{M_{\mathrm{s}}}\right). \tag{3}$$

The red dots are obtained directly from the data, which does not cause any problem for large values of B_{e}, but becomes difficult near the origin, where both B_{e} and M are small. A careful calibration of the offset of the measured magnetization field is therefore crucial here. We do that by fitting a second order curve

$$M = a_0 + a_1 B + a_2 B^2, \text{ with parameters } a_0, a_1, a_2$$

to the data in a neighborhood of the polarizing field where the measured magnetization changes sign. The correction term for the magnetic field data is then obtained as

$$B_{\mathrm{offset}} = -\frac{a_1}{2a_2} \pm \sqrt{\frac{a_1^2}{4a_2^2} - \frac{a_0}{a_2}}.$$

The smaller one of these two solutions is subtracted from the measured values of the polarizing field to ensure that the average magnetization is very close to zero for $B_{\mathrm{e}} = 0$. Note that this method does even work when the magnetization data contain hysteresis, provided that the magnetization curve is measured in both directions. This was indeed done for the measurement presented here.

The solid blue line in Fig. 1(b), on the other hand, is obtained from the quad-disperse fitting function. Its analytic representation causes no problem with regard to taking the ratio of two small numbers. The solid line agrees fairly well with the discrete values obtained directly from the data. The comparison brings out a small asymmetry with respect to the sign of the polarizing field for the discrete data points, which the symmetric ansatz for the quad-disperse fitting function cannot produce.

The maximum value of the effective magnetic moment corresponds to the arithmetic mean of the magnetic moments of the particles m_{a}, and the asymptotic value for large B_{e} to the harmonic mean m_{h}, as explained in more detail in Ref. [1].

Their difference $m_{\mathrm{a}} - m_{\mathrm{h}}$ is a direct order parameter for the amount of polydispersity: It is zero for a monodisperse distribution and increases with the width of the distribution. In fact, this difference divided by the harmonic mean provides an estimator for the relative standard deviation (RSD, also called coefficient of variation c_{v}). More precisely, we obtain the coefficient of variation as

$$c_{\mathrm{v}} = \sqrt{\frac{m_{\mathrm{a}} - m_{\mathrm{h}}}{m_{\mathrm{h}}}}. \tag{4}$$

Its value is listed in the upper part of Fig. 1(b).

Additionally, an estimator for the geometric mean is obtained by

$$m_{\mathrm{g}} = \sqrt{m_{\mathrm{a}} m_{\mathrm{h}}}. \tag{5}$$

It is provided in the figure as well, and its value is indicated by the blue arrow pointing to the corresponding location on the vertical axis.

Note that the calculations leading to c_{v} and m_{g} are only correct for certain distribution functions. Among those is the log-normal distribution, which seems to be the most prominent one assumed within the granulometric analysis of magnetization curves. It should be noted that the log-normal distribution tends to overestimate the fraction of large particles [7]. An alternative comparison with a gamma distribution is presented in Ref. [1].

The small differences between the data and the fitted curve in Fig. 1(b) become more prominent in Fig. 1(c), where the effective magnetic moment

$$m_{\mathrm{ta}} = k_{\mathrm{B}} T \frac{\partial}{\partial B_{\mathrm{e}}} \mathrm{L}^{-1}\left(\frac{M}{M_{\mathrm{s}}}\right), \tag{6}$$

obtained from the tangential slope, is shown [1]. Here the noise of the discrete data points is clearly larger. However, even here the signal/noise ratio seems good enough to extract the numbers for m_{a} and m_{h}, and the corresponding guesses for the geometric mean m_{g} and the relative standard deviation c_{v}.

3. Conclusion

We propose the superposition of a few – in our case four – Langevin curves as an effective and precise model to describe the magnetization curve of real ferrofluids. The four effective magnetic moments in that fit should not be over-interpreted in the sense that they represent a distribution function of the magnetic moments. However, two characteristic values of that function, namely the arithmetic and the harmonic mean, can be safely read off from a plot of the slope of the inverse Langevin function of the magnetization data. This graphical magnetogranulometry is sufficient to get an estimate for the relative standard deviation of the distribution function of the magnetic moments.

Declaration of Competing Interest

The authors declare that they have no known competing financial interests or personal relationships that could have appeared to influence the work reported in this paper.

CRediT authorship contribution statement

Ingo Rehberg: Conceptualization, Methodology, Software, Writing - original draft. **Reinhard Richter:** Investigation, Methodology, Software, Writing - review & editing. **Stefan Hartung:** Visualization, Data curation, Validation, Writing - review & editing.

Appendix A. Supplementary data

Supplementary data associated with this article can be found, in the online version, athttps://doi.org/10.1016/j.jmmm.2020.166868.

References

[1] I. Rehberg, R. Richter, S. Hartung, N. Lucht, B. Hankiewicz, T. Friedrich, Measuring magnetic moments of polydisperse ferrofluids utilizing the inverse langevin function, Phys. Rev. B 100 (2019) 134425.

[2] International conference on magnetic fluids, 2019,https://premc.org/conferences/icmf-magnetic-fluids/.

[3] A. Völkel, A. Kögel, R. Richter, Measuring the Kelvin-Helmholtz instability, stabilized by a tangential magnetic field, submitted to JMMM, this issue, 2019.

[4] T. Friedrich, T. Lang, I. Rehberg, R. Richter, Spherical sample holders to improve the susceptibility measurement of superparamagnetic materials, Rev. Sci. Instr. 83 (2012) 045106-045106-7.

[5] A.O. Ivanov, S.S. Kantorovich, E.N. Reznikov, C. Holm, A.F. Pshenichnikov, A.V. Lebedev, A. Chremos, P.J. Camp, Magnetic properties of polydisperse ferrofluids: a critical comparison between experiment, theory, and computer simulation, Phys. Rev. E 75 (2007) 061405.

[6] SciPy.org, Scientific computing tools for python, 2019,https://www.scipy.org.

[7] A. Pshenichnikov, V. Mekhonoshin, A. Lebedev, Magnetogranulometric analysis of concentrated ferrocolloids, J. Magn. Magn. Mater. 161 (1996) 94–102.

Publication 3

Assembly of eight spherical magnets into a dotriacontapole configuration

Stefan Hartung, Felix Sommer, Simeon Völkel,
Johannes Schönke, Ingo Rehberg

Physical Review B 98, 214424
(DOI: 10.1103/PhysRevB.98.214424)

Reprinted with permission.
©2018 American Physical Society

My contribution (50 %) consists of writing the program for controlling the magnetic-flux density scanner setup, designing and conducting the vast majority of experiments, supervising the characterization of the magnets, analyzing the data, preparing all figures and tables and writing the manuscript.

Felix Sommer characterized the magnets **(5 %)**.

Simeon Völkel contributed (20 %) a prototype for the setup and fitting routines and discussed the results.

Johannes Schönke contributed (20 %) the analytical theory.

Ingo Rehberg contributed (5 %) the assembly time estimation and supervised the research as well as the writing of the manuscript.

PHYSICAL REVIEW B **98**, 214424 (2018)

Assembly of eight spherical magnets into a dotriacontapole configuration

Stefan Hartung,[1,*] Felix Sommer,[1] Simeon Völkel,[1] Johannes Schönke,[2,†] and Ingo Rehberg[1,‡]
[1]*Experimentalphysik V, Universität Bayreuth, D-95440 Bayreuth, Germany*
[2]*Okinawa Institute of Science and Technology Graduate University, Onna, Okinawa 904-0495, Japan*

(Received 30 August 2018; revised manuscript received 31 October 2018; published 13 December 2018)

The magnetic field of a cuboidal cluster of eight magnetic spheres is measured. It decays with the inverse seventh power of the distance. This corresponds formally to a multipole named a dotriacontapole. This strong decay is explained on the basis of dipole-dipole interaction and the symmetry of the ensuing ground state of the cuboidal cluster. A method to build such dotriacontapoles is provided.

DOI: 10.1103/PhysRevB.98.214424

I. INTRODUCTION

Within the forces determining the interplay of condensed matter, the dipole-dipole interaction can be considered as the most important one, because monopoles do not exist for neutral matter, and pure quadrupole, octopole, or hexadecapol interaction tends to be masked by induced dipole moments. While the interaction of quadrupoles is not too exotic [1] and includes examples from continuum mechanics [2], pure octopole or even higher order interaction is different. Here we demonstrate that the combination of eight dipoles in a simple cubic arrangement leads to a 32-pole or dotriacontapole.

The exploration of the cuboidal dipole arrangement discussed here is triggered by the investigation of magnetic nanoparticles, which have been reported to self-assemble into such configurations [3,4]. The most elementary cluster of this type contains only eight particles. It can also be assembled macroscopically as a cubic cluster from eight magnetic spheres, as indicated by the left-hand side inset of Fig. 1, and described previously [5,6]. The ground state of this arrangement is stable, and an interesting continuum [5,7]. In this state, the spheres attract each other by the magnetic interaction. The cuboidal arrangement is an attractor, provided that the spheres are brought sufficiently close to that configuration and are allowed to adjust their orientation towards the ground state, i.e., their mutual friction must not be too large. That is the reason why the arrangement shown by the left-hand side inset of Fig. 1 can be assembled without needing a tremendous amount of dexterity, and in that sense the arrangement can be considered as almost self-assembled.

While the hallmark of a dipole is its field decay with the third power of the distance, the combination of eight dipoles could be expected to form a 16-pole or hexadecapole with a decay according to the sixth power. Amazingly enough, it turns out that the ground state of a cuboidal cluster of eight dipoles shows a field decay with the seventh power. This is explained by the symmetry of the ensuing ground state which make all lower-order terms vanish.

II. EXPERIMENTAL RESULTS

For reaching the ground state of the cluster, the eight spheres should be allowed to rotate freely. For that purpose it is useful to provide a Teflon® spacer to reduce the friction of the spheres, as shown in the right-hand side inset of Fig. 1. Here, the eight neodymium magnets of diameter $d = (19 \pm 0.05)$ mm are arranged in a cuboidal configuration by the holes at the corners of the white Teflon® cube, and kept at an edge length $L = (39.5 \pm 0.05)$ mm by means of the nonmagnetic Teflon® spacer. A hole is drilled into that spacer along the face diagonal, the (1,1,0) direction of the cube. This allows us to move the Hall probe (the black tip) into the cuboid, down to its center, by means of a stepper motor, using 0.1-mm steps. We adjust the spheres within their continuous ground state to maximize the measured magnetic-flux density. This is achieved by manually turning just one sphere around the space diagonal as rotation axis; the other ones follow accordingly due to the magnetic interaction.

The measured magnetic-flux density along the (1,1,0) direction is shown in Fig. 1. It has a maximum at about $r = 28$ mm—where the Hall probe is closest to the spheres—and decays to zero both when approaching the center, and when increasing the distance from the cube. The solid line corresponds to a fit of the numerical superposition of the flux densities of eight accordingly arranged point dipoles, as given by (1) discussed below.

The most important feature of this cuboidal arrangement of dipoles is the unusually steep decrease of the magnetic-flux density outside the cube. To quantify this decrease, Fig. 2 shows the data from Fig. 1 in a logarithmic plot. It becomes obvious that the magnetic-flux density decays with the inverse seventh power of the distance. To characterize this magnetic cluster with an appropriate name, it must be recalled that the field of dipoles decays with the third power, quadrupoles with the fourth power, and so on. In that sense, the seventh power corresponds to a dotriacontapole.

The fact that the field is expected to be zero at that center of the arrangement is caused by the symmetry of the

---

[*] Stefan.Hartung@uni-bayreuth.de

[†] Johannes.Schoenke@oist.jp

[‡] Ingo.Rehberg@uni-bayreuth.de

©2018 American Physical Society

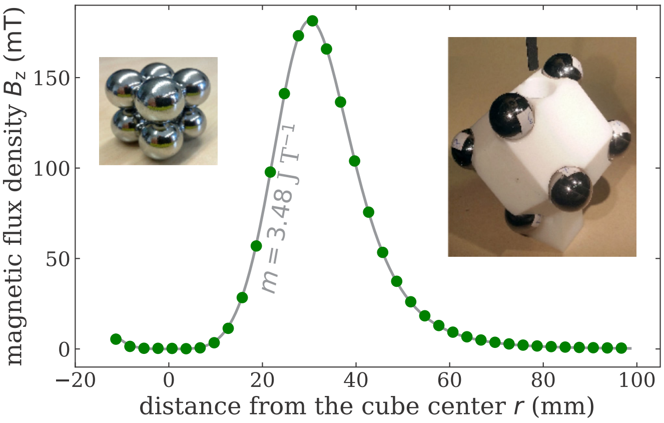

FIG. 1. Magnetic-flux density as measured along a straight path through the center of the cuboid. Only every 30th data point is shown. The solid line corresponds to the numerical superposition of the flux densities of eight accordingly arranged point dipoles with a magnetic moment $m = 3.48\ \mathrm{J\,T^{-1}}$. The left-hand side inset shows the principal cuboidal arrangement of the eight magnetic spheres, and the right-hand side inset a geometrically similar arrangement, but here with a white Teflon® spacer. The hole in that spacer allows us to take data inside the cuboid by means of the Hall probe, which is visible as the black part above the hole.

ground state. The measured deviations from that value can be attributed to geometrical and experimental imperfections: The dipole moments are not mathematically identical; they might not have reached their ground state due to the finite amount of friction, and the Hall probe can reach the center of the arrangement only with a mm precision.

The increase of the flux density with the fourth power is in agreement with the numerical evaluation of the ground state. According to that simulation, it even seems to be universal, i.e., independent of the direction along which the field is calculated. Compared to the seventh power of the decay this fourth power seems less exotic. It is somehow reminiscent of the field near the center of a Helmholtz pair of coils, where the second-order terms vanish at a singular value of the coil distance.

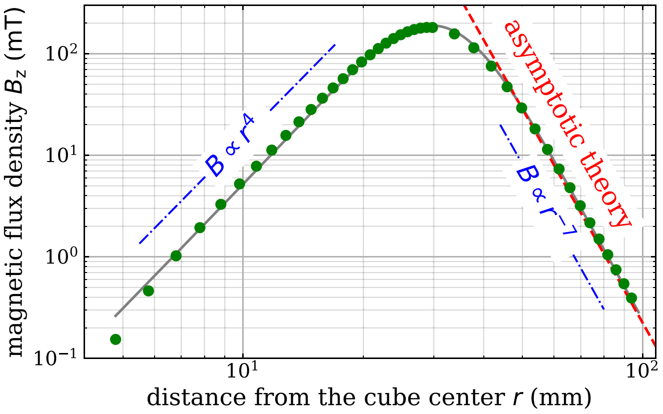

FIG. 2. The magnetic-flux density measured along a path starting from the center of the cuboid is represented by the circles. Only every tenth data point is shown at the left-hand side of the maximum, and every 40th data point at the right-hand side. The solid line is the same numerically obtained curve as in Fig. 1. The dash-dotted lines are for comparison with the expected asymptotic slopes. The dashed line depicts the analytical solution (7) for the far field.

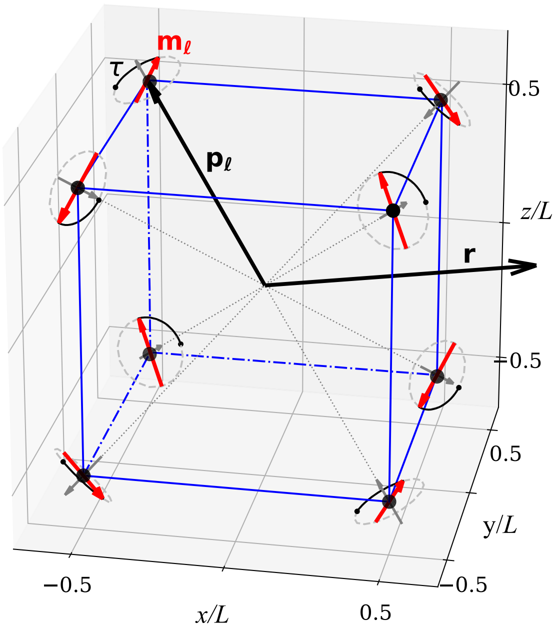

FIG. 3. The position $\mathbf{r}$ and the position vectors $\mathbf{p}_\ell$ of the dipole moments $\mathbf{m}_\ell$ are taken from the center of the cluster. The orientations of the dipoles in the continuous ground state are determined by the angle τ. The dipole configuration is sketched here for $\tau = 90^\circ$, which corresponds to the largest negative value of B_z along the (1,1,0) direction.

III. THEORY

The scalar potential ϕ at position $\mathbf{r}$ for a distribution of N dipoles with position vectors $\mathbf{p}_\ell$ and dipole moments $\mathbf{m}_\ell$ (see Fig. 3) is given by

$$\phi = \sum_{\ell=1}^{N} \frac{\mathbf{m}_\ell \cdot (\mathbf{r} - \mathbf{p}_\ell)}{4\pi |\mathbf{r} - \mathbf{p}_\ell|^3}. \tag{1}$$

This equation is expected to describe the cluster field, because the individual spheres have a pure dipole field, in agreement with the theoretical expectation for homogeneously magnetized spheres [8] and our measurements presented in Appendix A. The numerical results of this equation correspond to the gray lines in Figs. 1 and 2.

To explain the behavior of the magnetic-flux density $\mathbf{B}$ in the far field, we perform a *multidipole* expansion, where the potential is expanded in a series for $|\mathbf{p}_\ell| \ll |\mathbf{r}|$,

$$\phi = \sum_{\nu=0}^{\infty} \frac{1}{\nu!} \sum_{\ell=1}^{N} \left.\frac{\partial^\nu \phi}{\partial \mathbf{p}_\ell^\nu}\right|_{\mathbf{p}_\ell = 0} \cdot \underbrace{(\mathbf{p}_\ell \otimes \cdots \otimes \mathbf{p}_\ell)}_{\nu \text{ times}}.$$

As an example, the quadrupole (second term in the expansion) reads

$$\begin{aligned}\phi^{(2)} &= \frac{1}{4\pi |\mathbf{r}|^5} \sum_{\ell=1}^{N} [3(\mathbf{m}_\ell \cdot \mathbf{r})\mathbf{r} - |\mathbf{r}|^2 \mathbf{m}_\ell] \cdot \mathbf{p}_\ell \\ &= \frac{1}{4\pi |\mathbf{r}|^5} \sum_{\ell=1}^{N} \underbrace{[3\,\mathbf{m}_\ell \otimes \mathbf{p}_\ell - (\mathbf{m}_\ell \cdot \mathbf{p}_\ell)\mathbf{I}]}_{\mathcal{M}^2} \cdot (\mathbf{r} \otimes \mathbf{r}),\end{aligned}$$

with the second-order unit tensor $\mathbf{I}$. The second-order tensor $\boldsymbol{\mathcal{M}}^2$ is the quadrupole moment. Using Cartesian coordinates $\mathbf{p}_\ell = (p_\ell^x, p_\ell^y, p_\ell^z)$, $\mathbf{m}_\ell = (m_\ell^x, m_\ell^y, m_\ell^z)$ and $\mathbf{r} = (x, y, z)$, we obtain

$$\phi^{(2)} = \frac{1}{4\pi|\mathbf{r}|^5}\left[\underbrace{\sum_{\ell=1}^{N}\left(2p_\ell^x m_\ell^x - p_\ell^y m_\ell^y - p_\ell^z m_\ell^z\right)}_{\mathcal{M}^2_{200}} x^2 + 3\underbrace{\sum_{\ell=1}^{N}\left(p_\ell^x m_\ell^y + p_\ell^y m_\ell^x\right)}_{\mathcal{M}^2_{110}} xy + \cdots\right].$$

$\mathcal{M}^2_{ijk}$ are the Cartesian components of the moment $\boldsymbol{\mathcal{M}}^2$ with $i + j + k = 2$. Using the moments, the potential can be written as

$$\phi = \sum_{\alpha=1}^{\infty}\phi^{(\alpha)} = \sum_{\alpha=1}^{\infty}\frac{1}{4\pi|\mathbf{r}|^{2\alpha+1}}\sum_{i+j+k=\alpha}\mathcal{M}^\alpha_{ijk}\, x^i y^j z^k. \quad (2)$$

The cube ground state [5,9] is a highly shielded structure. For a cube with edge length L and dipole moment magnitudes $|\mathbf{m}_\ell| = m$ we have

$$\begin{aligned}
&\text{(dipole)} && \mathcal{M}^1_{ijk} = 0,\\
&\text{(quadrupole)} && \mathcal{M}^2_{ijk} = 0,\\
&\text{(octopole)} && \mathcal{M}^3_{ijk} = 0, && (3)\\
&\text{(hexadecapole)} && \mathcal{M}^4_{ijk} = 0,\\
&\text{(dotriacontapole)} && \mathcal{M}^5_{311} = C\,\sin(\tau + \pi/3),
\end{aligned}$$

$$\mathcal{M}^5_{131} = C\,\sin(\tau + 5\pi/3), \quad (4)$$

$$\mathcal{M}^5_{113} = C\,\sin(\tau + 9\pi/3), \quad (5)$$

where $\tau = 0\ldots 2\pi$ is the current phase angle [5,9] of the continuous ground state as indicated in Fig. 3 and Appendix B, and $C = 105\sqrt{3/2}\,L^4 m$. There are restrictions for the cube moments following from the symmetries of the ground state [5]. The potential ϕ has to be zero in the three planes, $x = 0$, $y = 0$, $z = 0$, as well as on the four volume diagonals, $|x| = |y| = |z|$. Together with (2) this leads to conditions for the nonzero moments $\mathcal{M}^\alpha_{ijk}$:

$$i, j, k \text{ positive, odd} \Rightarrow \alpha \text{ odd, and} \quad \sum_{i+j+k=\alpha}\mathcal{M}^\alpha_{ijk} = 0.$$

This explains why the first nonzero moments appear in the dotriacontapole,

$$\phi^{(5)} = \frac{\mathcal{M}^5_{311}\,x^3yz + \mathcal{M}^5_{131}\,xy^3z + \mathcal{M}^5_{113}\,xyz^3}{4\pi|\mathbf{r}|^{11}}. \quad (6)$$

The magnetic-flux density is related to the potential through $\mathbf{B} = -\mu_0\partial\phi/\partial\mathbf{r}$. We parametrize the measurement along the direction (1,1,0) with the radius parameter s through $(x, y, z) = (s, s, 0)/\sqrt{2}$ and obtain the following expression for the z component of the magnetic-flux density from (3)–(6):

$$\begin{aligned}
B_z(s,\tau) &= -\mu_0\frac{\partial\phi}{\partial z}\bigg|_{x=y=s/\sqrt{2},\, z=0}\\
&= -\frac{105\sqrt{3/2}\,\mu_0 L^4 m\,\sin\tau}{16\pi s^7} + \mathcal{O}\left(\frac{1}{s^9}\right). \quad (7)
\end{aligned}$$

The next order decays with $|\mathbf{B}| \propto 1/s^9$ because all moments with even α are zero.

Equation (7) is displayed in Fig. 2 by the dashed line. The solid lines in Figs. 1 and 2 are obtained numerically from the exact (1), with $\tau = 90^\circ$ taken as the phase angle of the continuous ground state (see Appendix C). It is amazing that this asymptotic prediction reaches the exact solution already at a distance of about 50 mm, which can be considered as sheer luck from an experimental point of view, because the field is hardly detectable for our equipment at distances larger than 100 mm. For the measurements shown there, the angle τ was adjusted manually to obtain the largest signal of the Hall probe to achieve an optimal signal-to-noise ratio. This corresponds either to $\tau = 90^\circ$ or to $\tau = 270^\circ$.

Note that the shape of the $B(r)$ curve shown in Figs. 1 and 2 is not universal, it rather depends on the direction of the line along which the flux density is measured. The $1/r^7$ decay, however, is a universal feature for all directions in the far-field limit, $|\mathbf{p}_\ell| \ll |\mathbf{r}|$.

IV. CONCLUSION AND OUTLOOK

In summary, we have demonstrated that eight spherical permanent magnets assemble into a configuration which behaves like a dotriacontapole. This can be explained by a model based on pure dipole-dipole interaction. This model is based on symmetry considerations which are an idealization of the experimental situation. The measurements make it clear that the conclusions drawn from the idealization are robust against (small) distortions, in particular the decay of the magnetic-flux density with $1/r^7$—a hallmark for a highly shielded structure—survives.

This finding implies that storing strong magnets in a cubic packing might be the optimal way for suppressing their field in the outer surrounding. Moreover, the extremely steep field decay has remarkable consequences for the clustering dynamics: If two dipole spheres, initially separated by say ten diameters, needed one second to collide due to their attractive force, for dotriacontapoles of comparable strength, this process would take more than one year (see Appendix B). Thus, dipoles which manage to arrange themselves in this configuration are fairly robust against further clustering. This argument is scale invariant. It applies to macroscopic granules in the early stages of planet formation [10], but could also shed some light on the self-assembly dynamics of colloidal nanomagnets [3,4] used for medical applications [11].

The plastic spheres shown in Fig. 4 demonstrate an attempt to build a handful of such dotriacontapoles with the help of a three-dimensional (3D) printer. Each sphere contains eight magnetic dipoles in a cubic arrangement. This is provided by three perpendicular walls inside these spheres, indicated in the left-hand side inset, and eight holes along the space

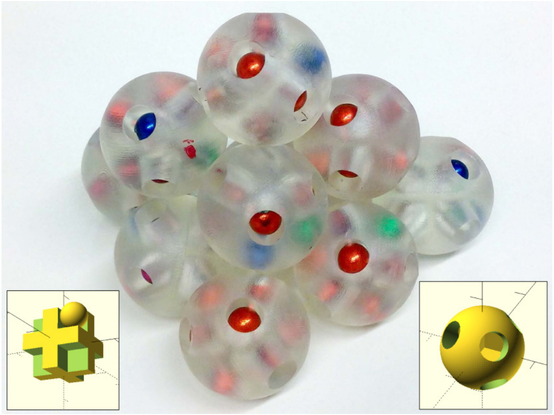

FIG. 4. A cluster of 3D-printed dotriacontapoles. The inner part of these spheres contains three perpendicular walls as indicated by the left-hand side inset. The colored magnetic spheres of 5 mm diameter are placed inside these plastic spheres by the eight holes along the space diagonals, as indicated by the right-hand side inset.

diagonals, as indicated by the right-hand side inset. These plastic spheres should thus interact with an extremely short-ranged interaction force, which should asymptotically decay with the inverse 12th power of the mutual distance—provided that the magnetic dipoles inside a sphere are in their ground state. Measuring such a short-range interaction between dipole clusters provides a challenge left to be faced in future work.

ACKNOWLEDGMENTS

It is a pleasure to thank F. Braun, K. Huang, R. Richter, W. Schöpf, and A. Weber for valuable hints and discussions. This work has been supported by the Deutsche Forschungsgemeinschaft (DFG) - Project No. 389197450.

APPENDIX A: MAGNETIC SPHERES AS DIPOLES

The magnetic spheres (MK-19-C from magnets4you GmbH) have a diameter of $d = (19 \pm 0.05)$ mm. For explaining the experimental findings with a theoretical model based on pure dipole-dipole interaction, it is crucial to demonstrate that these spheres can be described as magnetically hard point dipoles. Thus, we have measured the axial component of the magnetic-flux density B_x of a single sphere along the x direction in a 170-mm × 20-mm xy plane, as shown in the inset of Fig. 5. The flux density is measured by a Hall probe (HU-ST1-184605, MAGNET-PHYSIK Dr. Steingroever GmbH). The 3D positioning of this probe is done with a stepper motor (High-Z S-400T, with Zero-3 controller from CNC-STEP), the interface (CNCPod) is programmable in G-Code, DIN/ISO 66025. A single-board microcontroller (Leonardo, Arduino) is additionally used for interfacing it to a PC.

To emphasize deviations from the point dipole approximation, and to extract the underlying magnetic moment, we make use of the theoretically expected flux density of a point dipole [8],

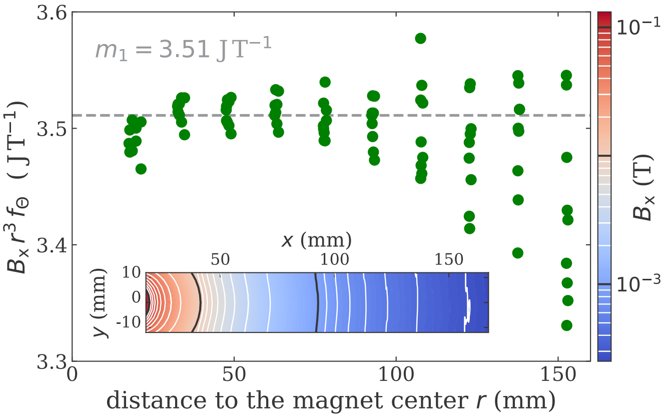

FIG. 5. The inset shows $B_x(x, y)$ measured in a plane, color coded in red for strong fields to blue for weak ones. The direction of the x coordinate is chosen to be parallel to the dipole moment $\mathbf{m}$ and forms a horizontal plane with the perpendicular coordinate y. An estimator for the magnetic moment is obtained from these data with (A2). The result is displayed as a function of r by the circles. The dashed line represents the mean value m_1 of these data.

$$B_x = \frac{\mu_0}{4\pi} \frac{m\,(3\cos^2\Theta - 1)}{r^3}, \tag{A1}$$

with $\Theta = \arctan(y/x)$, $r = \sqrt{x^2 + y^2}$ measuring the angle between the dipole moment and the position vector, and the magnetic constant μ_0. With the shorthand notation $\frac{4\pi}{\mu_0(3\cos^2\Theta - 1)} = f_\Theta$, this provides the magnitude of the magnetic moment,

$$m = B_x r^3 f_\Theta. \tag{A2}$$

The resulting m as a function of the measured value of $B_x(x, y)$ is plotted in Fig. 5 as a function of the distance of the Hall probe from the center of the sphere. The increasing

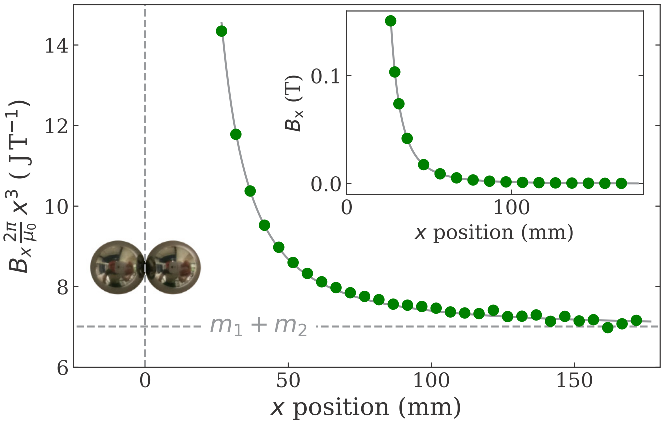

FIG. 6. Data obtained from the measurements of the magnetic-flux density B_x of two spheres in contact. The raw data are shown in the inset, and the solid line shows the calculated superposition of two dipole fields. B_x scaled with $x^3 2\pi/\mu_0$ is shown in the larger plot. The horizontal dashed line represents the sum of the magnetic moments of the isolated spheres. The dashed vertical line represents the origin at the contact point of the spheres.

scatter at larger distances r is caused by the fast decay of the magnetic-flux density. Based on these data, it seems safe to conclude that the point dipole approximation for the magnetic-flux density of the sphere is reliable within $\pm 2\,\%$. The mean value is $(3.51 \pm 0.18)\,\mathrm{J\,T^{-1}}$, which is well within the $(3.54 \pm 0.11)\,\mathrm{J\,T^{-1}}$ claimed by the manufacturer. We have measured all eight dipoles used in the experiments described here in a similar way, they differ by an amount of $\pm 3\%$.

To measure the mutual influence of such magnetic spheres, we brought them in direct contact as shown in the left-hand side inset of Fig. 6. The measured flux density along the axis of the resulting two-dipole cluster is shown as the right-hand side inset in Fig. 6. The position of the Hall probe is measured as the distance from the center between the spheres. The data reveal roughly the typical $1/x^3$ descent of a dipole, but deviations from that scaling are hard to judge from this inset plot. To get a better resolution for the deviations from the overall $1/x^3$ decay, the data were multiplied with x^3. After scaling with $2\pi/\mu_0$ one gets an estimate for the magnetic moment, which is displayed on the vertical axis of Fig. 6. These scaled data decay monotonically with the position x and reach the value of the sum of the two magnetic moments asymptotically, which is indicated by the dashed line. The solid line is the theoretical estimation, based on the superposition of the fields of the individually measured moments $m_1 = 3.51\,\mathrm{J\,T^{-1}}$ and $m_2 = 3.50\,\mathrm{J\,T^{-1}}$, with their mutual distance given by the diameter of the spheres. The good agreement between this curve and the data indicates that the magnets are hard ones: Their magnetic moment stays constant even under the influence of the immediately adjacent other magnet, at least within the experimental resolution on a percentage level.

APPENDIX B: DIPOLE ORIENTATION IN THE CUBE GROUND STATE

The dipole orientation within the ground state of the cuboidal cluster can be parametrized by a single parameter, namely the phase angle $\tau = 0^\circ \ldots 360^\circ$ [5,9]. The configuration for the angle $\tau = 90^\circ$ is illustrated in Fig. 3. The source code of a Python script animating this state together with the corresponding fields for adjustable values of τ is available [12]. The exact positions and orientations of the dipoles with respect to τ are provided by Table I.

TABLE I. Description of $\mathbf{p}_i$ and $\mathbf{m}_i$ in the cube ground state.

i	$\mathbf{p}_i$	$\mathbf{m}_i \cdot \sqrt{3/2}/m$
1	$\begin{pmatrix} 0.5 \\ 0.5 \\ 0.5 \end{pmatrix}$	$\begin{pmatrix} -\sin(\tau - 240^\circ) \\ -\sin(\tau - 120^\circ) \\ -\sin(\tau) \end{pmatrix}$
2	$\begin{pmatrix} 0.5 \\ 0.5 \\ -0.5 \end{pmatrix}$	$\begin{pmatrix} +\sin(\tau - 240^\circ) \\ +\sin(\tau - 120^\circ) \\ -\sin(\tau) \end{pmatrix}$
3	$\begin{pmatrix} 0.5 \\ -0.5 \\ 0.5 \end{pmatrix}$	$\begin{pmatrix} +\sin(\tau - 240^\circ) \\ -\sin(\tau - 120^\circ) \\ +\sin(\tau) \end{pmatrix}$
4	$\begin{pmatrix} 0.5 \\ -0.5 \\ -0.5 \end{pmatrix}$	$\begin{pmatrix} -\sin(\tau - 240^\circ) \\ +\sin(\tau - 120^\circ) \\ +\sin(\tau) \end{pmatrix}$
5	$\begin{pmatrix} -0.5 \\ 0.5 \\ 0.5 \end{pmatrix}$	$\begin{pmatrix} -\sin(\tau - 240^\circ) \\ +\sin(\tau - 120^\circ) \\ +\sin(\tau) \end{pmatrix}$
6	$\begin{pmatrix} -0.5 \\ 0.5 \\ -0.5 \end{pmatrix}$	$\begin{pmatrix} +\sin(\tau - 240^\circ) \\ -\sin(\tau - 120^\circ) \\ +\sin(\tau) \end{pmatrix}$
7	$\begin{pmatrix} -0.5 \\ -0.5 \\ 0.5 \end{pmatrix}$	$\begin{pmatrix} +\sin(\tau - 240^\circ) \\ +\sin(\tau - 120^\circ) \\ -\sin(\tau) \end{pmatrix}$
8	$\begin{pmatrix} -0.5 \\ -0.5 \\ -0.5 \end{pmatrix}$	$\begin{pmatrix} -\sin(\tau - 240^\circ) \\ -\sin(\tau - 120^\circ) \\ -\sin(\tau) \end{pmatrix}$

APPENDIX C: ASSEMBLY TIME FOR DIPOLES VERSUS THAT FOR DOTRIACONTAPOLES

The time T_{m} for two multipoles of diameter d starting at a distance of $10d$ to come into contact under the influence of their mutual attraction—a characteristic time for the dynamics of the self-assembly of magnetic clusters [3,4]—is obtained by integrating over their inverse velocity. When assuming that these particles are suspended in a viscous fluid, that velocity is proportional to the attractive force (Stokes's law). T_2 denotes the pair of dipoles, T_{32} denotes the pair of dotriacontapoles. The attracting force of these multipole pairs is assumed to be the same when they are in contact at the distance of $1d$,

$$\frac{T_{32}}{T_2} = \frac{\int_{5d}^{d/2} \frac{1}{v_{32}}\,dr}{\int_{5d}^{d/2} \frac{1}{v_2}\,dr} \overset{v \propto F}{=} \frac{\int_{5d}^{d/2} -\left(\frac{2r}{d}\right)^{12} dr}{\int_{5d}^{d/2} -\left(\frac{2r}{d}\right)^{4} dr}$$
$$= \frac{5}{13}\,\frac{10^{13}-1}{10^{5}-1} \approx 0.4 \times 10^{8}.$$

This ratio turns, e.g., $1s$ for a dipole pair into $1a$ for the corresponding pair of dotriacontapoles: They are fairly robust against further clustering.

[1] A. D. Buckingham, Q. Rev., Chem. Soc. **13**, 183 (1959).

[2] D. Stamou, C. Duschl, and D. Johannsmann, Phys. Rev. E **62**, 5263 (2000).

[3] S. Mehdizadeh Taheri, M. Michaelis, T. Friedrich, B. Förster, M. Drechsler, F. M. Römer, P. Bösecke, T. Narayanan, B. Weber, I. Rehberg, S. Rosenfeldt, and S. Förster, Proc. Natl. Acad. Sci. USA **112**, 14484 (2015).

[4] S. Rosenfeldt, S. Förster, T. Friedrich, I. Rehberg, and B. Weber, in *Novel Magnetic Nanostructures*, Advanced Nanomaterials, edited by N. Domracheva, M. Caporali, and

E. Rentschler (Elsevier, Amsterdam, Netherlands, 2018), pp. 165–189.

[5] J. Schönke, T. M. Schneider, and I. Rehberg, Phys. Rev. B **91**, 020410 (2015).

[6] S. Borgers, S. Völkel, W. Schöpf, and I. Rehberg, Am. J. Phys. **86**, 460 (2018).

[7] P. I. Belobrov, R. S. Gekht, and V. A. Ignatchenko, Zh. Eksp. Teor. Fiz. **84**, 1097 (1983) [Sov. Phys. JETP **57**, 636 (1983)].

[8] J. D. Jackson, *Classical Electrodynamics*, 3rd ed. (Wiley, New York, 1999).

[9] J. Schönke, An interactive gallery of the dipole cube, http://ecps.ds.mpg.de/people/cube_gallery/cube_gallery.html (2015).

[10] J. Blum, Adv. Phys. **55**, 881 (2006).

[11] T. M. Buzug, J. Borgert, T. Knopp, S. Biederer, T. F. Sattel, M. Erbe, and K. Lüdtke-Buzug, *Magnetic Nanoparticles* (World Scientific, Singapore, 2010).

[12] I. Rehberg, Ground state of the dipole cube, http://www.staff.uni-bayreuth.de/∼bt180034/dotriacontapole.html (2018).

Publication 4

Dynamics of a magnetic gear with two cogging-free operation modes

Stefan Hartung and Ingo Rehberg

Archive of Applied Mechanics, 1-13 (2020)
(DOI: 10.1007/s00419-020-01830-z)

Reprinted with permission.
©The Author(s) 2020

My contribution (80 %) consists in conceptualizing the scope of the work, enhancing the existing experimental setup with a new library for the stepper motor for finer frequency tuning, establishing an electrical trigger for the camera in synchronization with the motor steps, conducting all experiments, creating figures 1-9, designing the theoretical model, creating the final programs for its numerical simulation and writing the majority of the manuscript.

Ingo Rehberg contributed (20 %) the initial numerical simulation of the theoretical model, a substantial part to the manuscript, the creation of figure 10 and supervision to the research in helpful discussion, for which I am very grateful.

Arch Appl Mech
https://doi.org/10.1007/s00419-020-01830-z

ORIGINAL

Stefan Hartung · **Ingo Rehberg**

Dynamics of a magnetic gear with two cogging-free operation modes

Received: 31 August 2020 / Accepted: 20 October 2020
© The Author(s) 2020

Abstract The coupling of two rotating spherical magnets is investigated experimentally. For two specific angles between the input and output rotation axes, a cogging-free coupling is observed, where the driven magnet is phase-locked to the driving one. The striking difference between these two modes of operation is the reversed sense of rotation of the driven magnet. For other angles, the experiments reveal a more complex dynamical behavior, which is divided in three different classes. This is done by analyzing the deviation from a periodic motion of the driven magnet, and by measuring the total harmonic distortion of this rotation. The experimental results can be understood by a mathematical model based on pure dipole–dipole interaction, with the addition of adequate friction terms.

Keywords Couplings · Gears · Permanent magnets · Permanent magnet machines · Rotating machines

1 Introduction

Magnetic gears have advantages: The input and output are free of mechanical contact. Thus, they are not subject to mechanical wear, need no lubrication, and operate with reduced maintenance. Moreover, they possess inherent overload protection, are noiseless, and highly reliable [1].

With the appearance of strong magnets based on alloys of rare-earth elements, the interest in magnetic gears based on permanent magnets grew because of increased torque transmission capabilities [2–5] and continues to do so today [6].

An interesting type of a magnetic gear based on pure magnetic dipoles has been proposed in 2015 by J. Schönke [7]. Inspired by his former work on a sevenfold magnetic clutch [8], he demonstrated theoretically that two magnetic dipoles could couple in two cogging-free modes, provided that the angles of the two rotation axes follow a certain algebraic condition. Almost pure dipoles are indeed commercially available in the form of spherical permanent magnets, as has been demonstrated experimentally [9]. A first experimental demonstration of the principle of this gear using such spherical magnets concentrated on static aspects [10]. In this paper, we provide measurements of the *dynamical* behavior of such a gear. Moreover, we compare these measurements with numerical simulations of the dynamics of two coupled magnetic dipoles.

S. Hartung ( ) · I. Rehberg
Experimental Physics V, University of Bayreuth, Bayreuth, Germany
E-mail: Stefan.Hartung@uni-bayreuth.de

I. Rehberg
E-mail: Ingo.Rehberg@uni-bayreuth.de

Published online: 06 November 2020

2 Experimental setup

Fig. 1 shows the experimental setup, which is very similar to the one described by Borgers et al. [10]. The two spherical neodymium permanent magnets have a diameter of 19 mm and are each attached to a shaft with their dipole moment aligned perpendicular to the rotation axis with a precision of about 3°. Both axes lie in the horizontal plane. The bearings are non-magnetic and electrically non-conducting. The input shaft runs in a bearing that consists of a plastic cage with glass beads, which has been constructed in our in-house workshop. It is connected to a stepper motor by an 80 cm long brass rod to suppress any magnetic interference between the motor and the spherical magnets. The output shaft runs in two industrial full ceramic deep groove ball bearings made out of silicon nitride, in which it can rotate freely [11].

To track the orientation of the dipole $\mathbf{m}_2$, the end of the output shaft is covered with a white surface marked with a black line which is recorded by a CCD-camera. The stepper motor and the CCD-camera are both connected to a computer. The input dipole angle α (see Fig. 2) is detected by a signal from the stepper motor yielding a resolution of 7.2°. The output dipole angle β is obtained by digitally processing the image of the black line marker. As an additional feedback to track α, a commercial wireless acceleration sensor is located on the brass rod that drives the input [12]. The position of the output shaft is fixed on a granite table, while the input shaft can be oriented freely on the surface of the table. An interchangeable spacer keeps the distance between the dipoles constant during a set of experiments, while the relative orientation of their rotation axes can be varied.

The system geometry is further explained in Fig. 2. The x-axis is determined by the connection between the two dipoles $\mathbf{r}_{12}$. The y-axis lies in the plane defined by $\mathbf{r}_{12}$ and the shaft axes. The results shown in this article stem from experiments with parallel rotation axes of input and output so that $\Theta \approx \Phi$ applies.

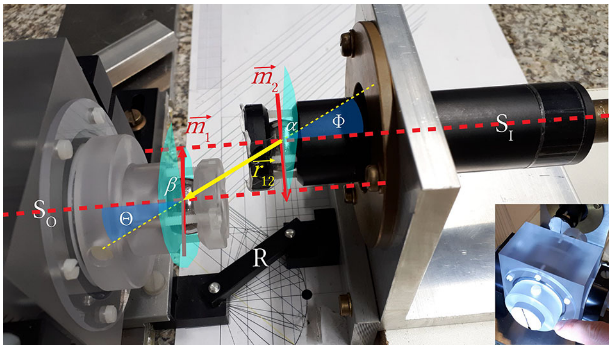

Fig. 1 Experimental setup: The input S_I and output S_O axis are marked by dashed red lines. The rotations of the magnetic moments $\mathbf{m}_1$ and $\mathbf{m}_2$ (red arrows) are marked by α and β. The spacer R keeps the distance $\mathbf{r}_{12}$ between the dipole centers. Their connecting line (dotted yellow) forms the input (output) shaft angle Θ (Φ) with the input (output) axis. The inset shows the marker for the optical data readout at the front end of S_O

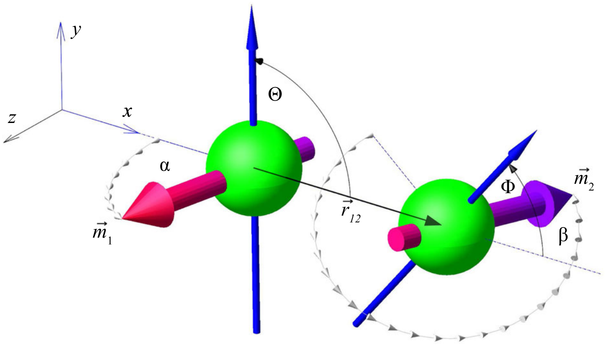

Fig. 2 Coordinate system defining the orientation angles. The x-axis connects the center of the input (left sphere) with that of the output magnet (right sphere). Their distance is $\mathbf{r}_{12}$. The rotation axes of the magnets (blue arrows) lie in the x-y-plane. Their angle toward the x-axis is Θ (Φ) for the input (output). The orientation of $\mathbf{m}_1$ and $\mathbf{m}_2$ (thick arrows) is marked by α and β measured against the x-y-plane

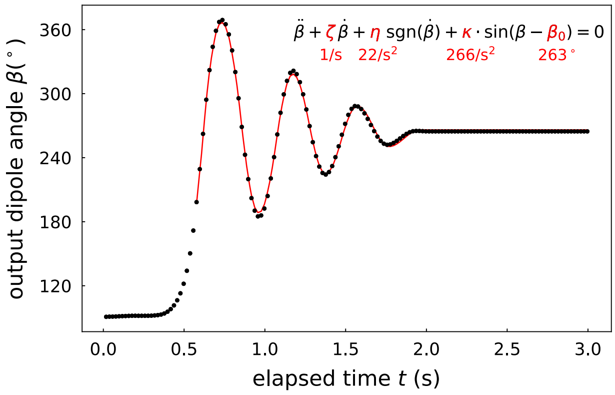

Fig. 3 Temporal evolution of β for a locked input angle α_0, and shaft angles $\Phi=\Theta=31°$. The elapsed time starts with the release of the output from the unstable equilibrium position. The formula in the top right is fitted (red curve) to the measured data points (black dots). Red letters show the fit parameters and their respective values

3 Quantifying system parameters

While the work of Borgers et al. focused on the static equilibrium conditions of a magnetic clutch [10], this article shows the dynamic behavior of the output when the input magnet is driven with a constant frequency. Thus, friction is an important additional parameter in our system which we determine experimentally by keeping the input angle fixed and analyzing the oscillation of the output around its equilibrium position. Following refs. [7,10], the equilibrium position for the angle β_0 of the output as a function of a fixed input angle α_0 can be written as

$$\beta_0 = \arctan\left(\frac{1}{\Delta}\tan(\alpha_0) + k\cdot\pi\right), \quad k \in \mathbb{N}_0. \tag{1}$$

Here, $\Delta \neq 0$ is the shaft orientation index of the input and output shaft angles Θ and Φ and writes as

$$\Delta = \cos\Theta\cos\Phi - 2\sin\Theta\sin\Phi. \tag{2}$$

In an ideal system without friction, the oscillation the output will undergo when turned out of its equilibrium position is therefore described by

$$\ddot{\beta} + \kappa\,\sin(\beta - \beta_0) = 0, \tag{3}$$

where κ is the restoring coefficient defined by

$$\kappa = \left(\frac{d\tau_{\mathrm{ax}}}{d\beta}\right)\cdot\frac{1}{I_{\mathrm{ax}}} = \frac{D}{I_{\mathrm{ax}}}. \tag{4}$$

Here, τ_{ax} is the torque on the output, I_{ax} is its moment of inertia, both along its rotation axis, and D is the directional constant. For any real coupling, however, this equation is unsatisfactory, since the ball bearings are prone to friction.

To quantify the influence of friction, we conduct a damped oscillation experiment in which the input rotation is prevented while the output magnet can rotate freely. We first turn the output magnet out of its equilibrium position until the restoring moment reaches its maximum. From there, we release the output magnet and record its damped oscillation with the camera. An exemplary result of such a measurement can be seen in Fig. 3. We make 20 such measurements, each with a different locked input angle α_0. The output and input shaft are parallel to each other with constant shaft angles $\Theta=\Phi=(31\pm 3)°$. The relatively high uncertainty stems from the fact, that a small tilt of the magnets in their sockets is difficult to avoid during their fixation in our setup, as well as small deviations from the parallel alignment.

We evaluate our model by fitting it to the data points. We find that the addition of a single, dry friction-related term is not sufficient to give a good representation of the experiment. The data implies that we need

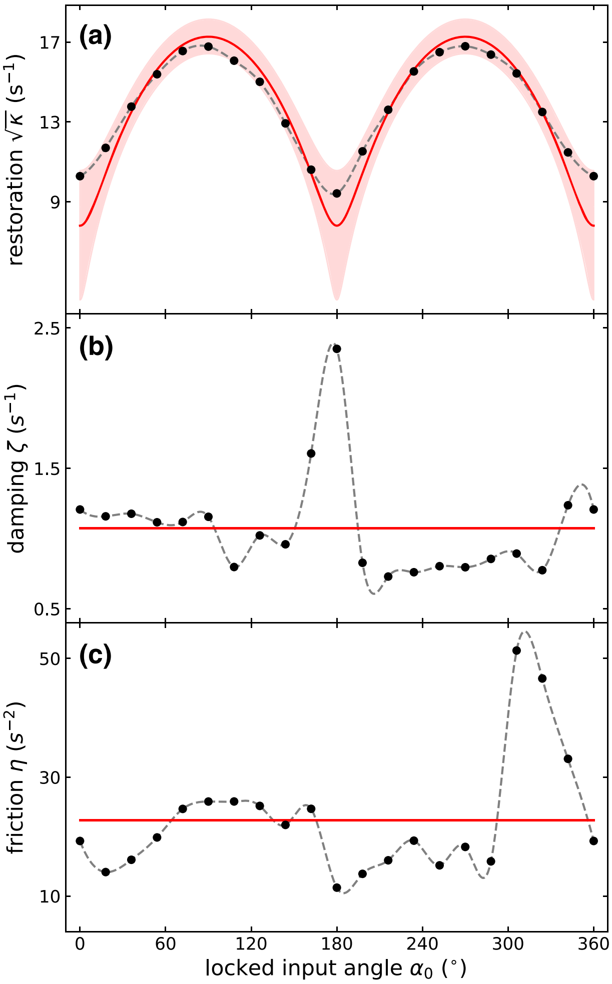

Fig. 4 Summary of the fit parameters (black dots) from damped oscillation experiments. The gray dotted lines are guides to the eye. In graph (a), the red line is the result of a theoretical calculation for $\Theta = 31°$ with its uncertainty shown by the red area. In (b) and (c), the red line indicates the arithmetic mean of the data points

another, rotation frequency-dependent friction parameter to describe the oscillation. By consideration of these aspects, (3) changes toward

$$\ddot{\beta} + \zeta \dot{\beta} + \eta \, \mathrm{sgn}(\dot{\beta}) + \kappa \, \sin(\beta - \beta_0) = 0. \tag{5}$$

Here, we call ζ the damping torque coefficient that takes account for the fluid-like friction in our system. The dry friction is represented by η, the friction torque coefficient, defined by

$$\eta = \frac{\tau_{\mathrm{fr}}}{I_{\mathrm{ax}}} = \frac{\mu \, F \, \frac{d_{\mathrm{cyl}}}{2}}{I_{\mathrm{ax}}}, \tag{6}$$

with τ_{fr} being the friction torque for a normal force F on the bearings, a rotating cylinder of diameter d_{cyl} and a sliding friction coefficient μ.

For a realistic model of the output response, we need estimates for the values of ζ and η. Therefore, we fit (5) to our sets of data for different α_0 with ζ, η, κ as the fit parameters. We decide to fit β_0 as well. This is more precise than calculating β_0 from (1). While the value of β_0 is not interesting, the obtained values of the other fit parameters are shown in Fig. 4 for the respective locked input angles.

The values obtained for $\sqrt{\kappa}$ are shown in the top panel. To compare them with a theoretical estimate, we calculate its value starting from (4). The torque τ is caused by the dipole–dipole interaction and reads

$$\boldsymbol{\tau} = \mathbf{m}_2 \times \mathbf{B}_1. \tag{7}$$

Here, $\mathbf{B}_1$ is the magnetic flux density of the input magnet

$$\mathbf{B}_1 = \frac{\mu_0}{4\pi} \frac{3\,(\mathbf{m}_1 \cdot \mathbf{r})\,\mathbf{r} - \mathbf{m}_1 r^2}{r^5}, \tag{8}$$

while the magnetic moment of the input magnet $\mathbf{m}_1$, of the output magnet $\mathbf{m}_2$ and the distance vector $\mathbf{r}$ are

$$\begin{aligned} \mathbf{m}_1 &= m_1 \begin{pmatrix} -\cos\alpha \sin\Theta \\ \cos\alpha \cos\Theta \\ \sin\alpha \end{pmatrix}, \\ \mathbf{m}_2 &= m_2 \begin{pmatrix} -\cos\beta \sin\Phi \\ \cos\beta \cos\Phi \\ \sin\beta \end{pmatrix}, \quad \mathbf{r} = r \begin{pmatrix} 1 \\ 0 \\ 0 \end{pmatrix}. \end{aligned} \tag{9}$$

Since the output can only rotate around the shaft axis, only the component τ_{ax} of the torque along the shaft is of interest. We calculate it as

$$\tau_{\mathrm{ax}} = \boldsymbol{\tau} \begin{pmatrix} \cos\Phi \\ \sin\Phi \\ 0 \end{pmatrix}. \tag{10}$$

With (2), (7), (8), (9) this becomes

$$\tau_{\mathrm{ax}} = \frac{\mu_0}{4\pi} \frac{m_1 m_2}{r^3} \left(-\sin\alpha \cos\beta + \Delta \cos\alpha \sin\beta \right). \tag{11}$$

The moment of inertia of the output shaft I_{ax} is difficult to estimate. Reasons for this are the spacers on both shaft ends, the additional moment of inertia from the bearing balls, and the different densities between the permanent magnet and the rest of the shaft material. We therefore treat it as a fit parameter in the calculation of κ. With (11), we get

$$\kappa = \frac{\mu_0 m_1 m_2}{4\pi r^3 I_{\mathrm{ax}}} \left(\sin\alpha_0 \sin\beta_0 + \Delta \cos\alpha_0 \cos\beta_0 \right) \tag{12}$$

We measured the magnetic dipole moments of the input and output in a former work as $m_1 = m_2 = (3.51 \pm 0.11)\,\mathrm{JT}^{-1}$ [9]. The distance between the magnets is $r = (40.0 \pm 0.5)$ mm. With this, we fit $\sqrt{\kappa}$ via I_{ax} according to (12) to the data for different α_0. The result is seen as the red line in the top panel of Fig. 4. The red shaded area marks the uncertainty of the fitted curve that stems from the variation of the constants within their measurement accuracy. The fitted value for the moment of inertia is

$$I_{\mathrm{ax}} = 6.45 \cdot 10^{-5}\,\mathrm{kgm}^2. \tag{13}$$

The complete output shaft has a mass of $m = (320 \pm 1)$ g, which corresponds to a radius of gyration of

$$r_{\mathrm{gyr}} = \sqrt{\frac{I_{\mathrm{ax}}}{m}} = 14.2\,\mathrm{mm}. \tag{14}$$

By approximating the output shaft as a circular cylinder and its mass to be homogeneous, its effective diameter is

$$d_{\mathrm{eff}} = 2 \frac{r_{\mathrm{gyr}}}{\sqrt{2}} = 40.16\,\mathrm{mm}. \tag{15}$$

This is a reasonable result, since the inside diameter of the bearings that hold the shaft is $d_{\mathrm{cyl}} = (30.0 \pm 0.1)$ mm and the diameter of the spacers on the shaft ends is $d_{\mathrm{spacer}} = (50.0 \pm 0.1)$ mm.

We see in Fig. 4 that the experimentally obtained values for κ are in good agreement with the theoretical prediction. Nevertheless, the fact that the red curve leads to systematically higher values at the maxima and lower values at the minima indicates that the actual shaft angles might be slightly smaller than what we measured at the spacer position.

The middle and bottom panels of Fig. 4 show the fitted values for ζ and η. Their relative variation is up to approximately 100%. Any dependence on α_0, however, we interpret as shortcomings of our setup that hold no further information. We therefore simply take the arithmetic means of both data sets, which are shown as the horizontal red line in the respective graph and get

$$\begin{aligned} \zeta &= (1.1 \pm 0.4)\,\mathrm{s}^{-1} \\ \eta &= (23.1 \pm 9.9)\,\mathrm{s}^{-2}. \end{aligned} \tag{16}$$

The sliding friction coefficient μ is determined from (16) and (13) and yields

$$\mu = \frac{\eta\, I}{F\, \frac{d_{\mathrm{cyl}}}{2}} = \frac{\eta\, d_{\mathrm{eff}}^2}{4\, g\, d_{\mathrm{cyl}}} = 0.031 \pm 0.014, \tag{17}$$

with g being the gravitational constant. For the dry sliding friction coefficient between two surfaces of silicon nitride ($\mathrm{Si_3N_4}$), the material of the bearing balls and cage, we find a way higher value of $\mu = 0.17$ in the literature [13–15]. However, one has to keep in mind that we calculated the friction coefficient for a system with rolling balls instead of sliding ones. Aramaki et al. investigated the friction of a $\mathrm{Si_3N_4}$ bearing and found that values for μ vary from 0.01 to 0.05 depending on the applied load and the spinning velocity of the balls [16]. This is in good agreement with our result.

4 Output response for finite driving frequencies

We now want to analyze the response of the output magnet while the input magnet is driven with a constant rotation frequency. From measuring β, we calculate the angle difference δ between input and output as

$$\delta = \beta - \alpha. \tag{18}$$

We do so for parallel rotation axes and different shaft angles $\Theta = \Phi$ and driving frequencies f.

Three examples of these measurements are shown for $\Theta = 31°$ in Fig. 5. Each of them features a unique response of the output. In the bottom panel, δ is periodic with a full rotation of the input, which we call T-periodic. The middle panel shows δ to be periodic with a half rotation of the input, i.e., $T/2$-periodic. In the top panel, the answer of δ is seemingly non-periodic, chaotic.

We find that after a short settling phase, each of our measurements falls in one of these categories. An objective tool for differentiation is by the method shown in the flowchart on the right-hand side of Fig. 5. We first make a multi-harmonic fit δ_{harm} to the data

$$\delta_{\mathrm{harm}} = \left(\sum_{i=1}^{7} a_i \sin i\,\alpha + b_i \cos i\,\alpha \right) + b_0 \tag{19}$$

with $a_{1,\ldots,7}$ and $b_{0,\ldots,7}$ as the fitting parameters. Here, $i = 1$ marks a response with the fundamental mode of the input while $i = 2, \ldots, 7$ are the respective higher harmonics. The first decision is done regarding whether the output behaves chaotically or is answering periodically. For this, we calculate the root mean square (RMS) of the difference between δ and δ_{harm} for the last 10 rotations of a measurement where 50 positions of α are detected for each rotation, namely

$$\mathrm{RMS} = \sqrt{\frac{1}{500} \sum_{m=4501}^{5000} (\delta_m - \delta_{\mathrm{harm}}(\alpha_i))^2}. \tag{20}$$

We find that RMS > 20 serves well to be characteristic for a chaotic output. To differentiate between T periodicity and $T/2$ periodicity, we calculate the total harmonic distortion ($\mathrm{THD_F}$) of δ_{harm} as

$$\mathrm{THD_F} = \frac{\sqrt{\sum_{i=2}^{7} (a_i^2 + b_i^2)}}{a_1^2 + b_1^2}. \tag{21}$$

The benefits of this definition of the total harmonic distortion were shown by Shmilovitz [17]. For $\mathrm{THD_F} = 1$, the amplitudes of all harmonic modes of δ together are just as big as the fundamental one. We use $\mathrm{THD_F} > 1$

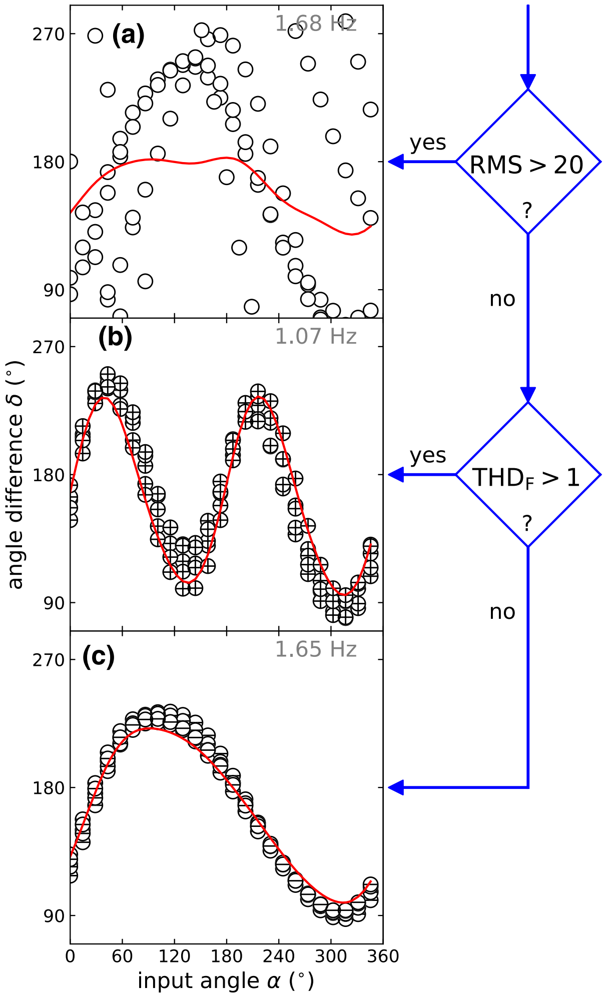

Fig. 5 Scheme for differentiating between three types of output rotation. The right-hand side shows a logical flowchart. On the left-hand side an exemplary graph for each kind is provided. α is depicted modulo 360°. For each plot, the response to the last 10 of 100 full rotations of the input is shown. Non-periodic response is marked in (**a**) by empty circles. Circled crosses in (**b**) denote $T/2$ periodicity, and circled dashes in (**c**) T periodicity. The red lines show the results of the harmonic fits (19) to the data points

to identify the case of $T/2$ periodicity. For smaller values, the fundamental mode prevails and δ is seen as T-periodic.

To further investigate the transition between these phases, δ is shown in Fig. 6 for different driving frequencies of the input f at constant shaft angles $\Theta = \Phi = 31°$. This way of presenting the data is adopted from the work of Borgers et al. [10]. It is explained by a more detailed diagram in the top part of Fig. 6.

The frequencies shown in the bottom part are chosen as such that the polar diagrams give a good representation of the phases observed in the experiment and displayed on the left-hand side. For each plot, the measurement started from the resting position of the input at $\alpha = 90°$ and the output at $\beta = 270°$. This is followed by a settling phase of 90 input rotations. The data that are shown stem from the next 10 input rotations.

For $f = 1.00$ Hz, the experimentally observed δ seems to behave chaotically. When f is increased up to 1.07 Hz, $T/2$ periodicity of δ is observed. The thickness of the line indicates the experimental noise. Both at 1.33 Hz and at 1.48 Hz $T/2$ periodicity can be seen as well—the pattern clearly is symmetric with a 180° turn of α. This is clearly not the case anymore for 1.63 Hz and 1.65 Hz where we enter the T-periodic regime. At 1.68 Hz, we observe seemingly chaotic behavior again.

Simulated results for δ are shown on the right-hand side for the respective driving frequencies. They were derived using a model similar to (5) except for a change in the last summand, because the magnetic torque is

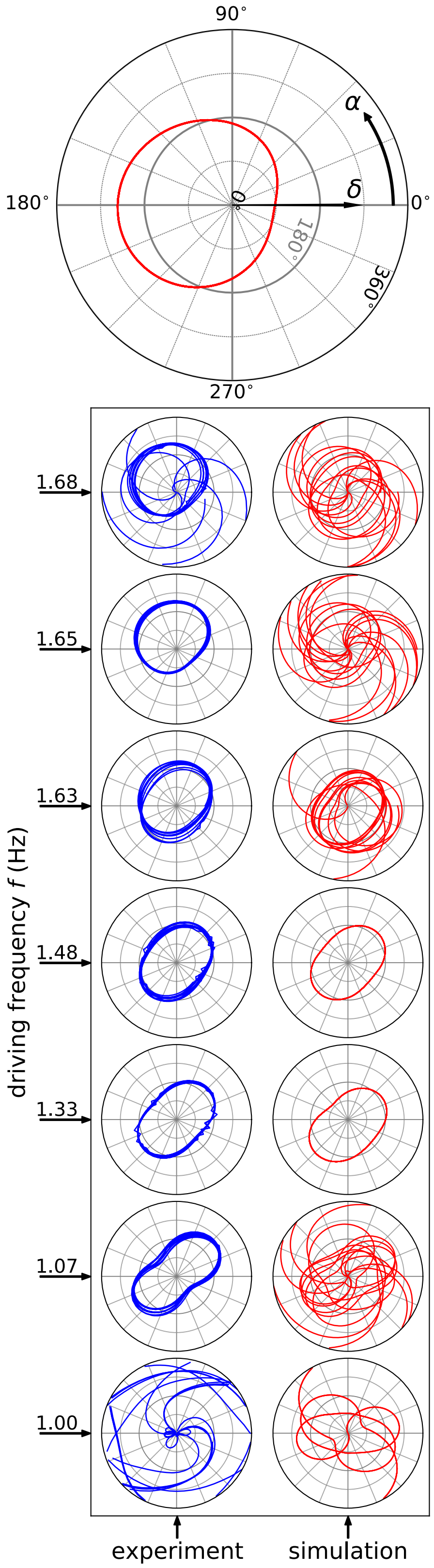

Fig. 6 Polar diagrams with radial distance δ and azimuthal angle α for different driving frequencies of the input ($\Theta = 31°$). The graphs each show the last 10 of 100 full rotations of input angle. Experimental results are shown in blue, the simulation in red. The top shows an expanded diagram simulated for 2.08 Hz. The arrows on the left-hand side mark the respective input driving frequencies

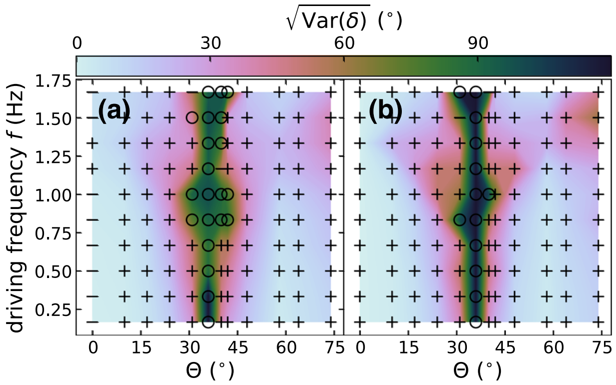

Fig. 7 Color map of the standard deviation of δ for different shaft angles Θ and driving frequencies f. **a** Shows experimental data, **b** stems from a numerical simulation. Each data point is represented by a marker: circles indicate chaotic response, crosses $T/2$ periodicity, and dashes T periodicity

now time-dependent. With the use of (11), (13) and (16), we get

$$\ddot{\beta} + \zeta \dot{\beta} + \eta \, \mathrm{sgn}(\dot{\beta}) + g_\tau \left(-\sin\alpha \cos\beta + \Delta \cos\alpha \sin\beta\right) = 0, \tag{22}$$

with

$$g_\tau = \frac{\mu_0}{4\pi} \frac{m_1 m_2}{I_{\mathrm{ax}} \, r^3}. \tag{23}$$

We solve this equation for β numerically, with discrete time steps

$$\Delta t = \frac{1}{n \, f}, \tag{24}$$

with f being the driving frequency of the input and $n = 50$.

For 1.00 Hz, the simulation differs qualitatively from the experiment: the response is 3 T-periodic. At 1.07 Hz, the simulation creates a chaotic response. We see a T-periodic response at 1.33 Hz and a $T/2$-periodic response at 14.8 Hz. For 1.63 Hz, 1.65 Hz and 1.68 Hz, the simulated data appears to be chaotic.

In a recent work of Haugen and Edwards, it was shown that the free oscillation of two magnetic dipoles in a plane does not feature chaotic behavior, contradictory to their own intuition [18]. This is not in contradiction with our findings here, because they did not take an externally driven magnet into account. This adds one degree of freedom to the system, thus allowing for chaotic motions.

In summary, both experiment and simulation create similar dynamical scenarios, but a quantitative match cannot be achieved due to the simplicity of our model.

In order to further investigate qualitative changes in the dynamics of the output magnet in our experiment, the measurement of δ is shown in Fig. 7 as a color map for different parallel shaft angles $\Theta = \Phi$ and driving frequencies f. The experimental data shown on the left-hand side can be compared to a simulation of (22) with appropriate parameters shown on the right-hand side. In both cases, phases of chaotic behavior are surrounded by periodic phases with high standard deviation of δ which stem from oscillations with high amplitudes.

The shaft angles near $\Theta = 0°$ and $\Theta = 54.74°$—the cogging-free cases [7,10]—are characterized by a minimum of $\mathrm{RMS}_\delta = \sqrt{\mathrm{Var}(\delta)}$. Once the shaft angles approach $\Theta = 35.26°$, we reach a maximum of this value. This is the position where the highest cogging occurs, accompanied by a change of the sense of rotation of output angle β. We conclude that the cogging of this magnetic gear is an important factor for the onset of chaotic motion.

It is interesting to note that the red highlighted area of higher oscillation amplitudes is widest spread at driving frequencies near $f = 1.3$ Hz. A possible reason for this could be the reaching of a resonance frequency of the output shaft. This might also explain why chaos is predominantly observed near that frequency.

While the experimental results summarized in Fig. 7 are restricted to the parameter range accessible in our experiment, we provide an expanded range in Fig. 8, where the data are based on purely numerical simulation. The whole range of shaft angles for parallel alignment is analyzed with increasing driving frequencies for each configuration that range from 0.1 Hz up to 100 Hz and is shown on a logarithmic scale.

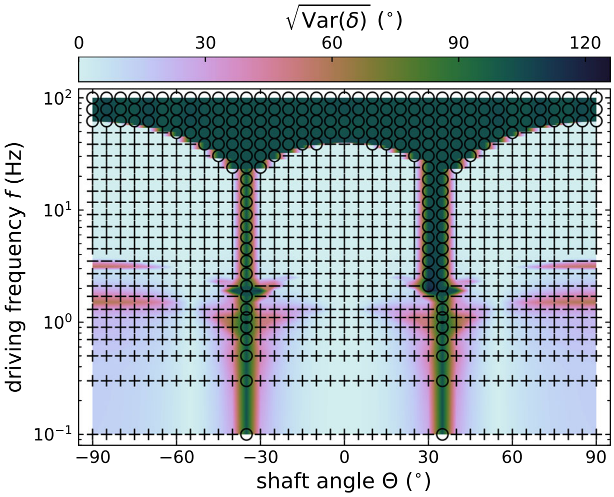

Fig. 8 Diagram similar to Fig. 7, but limited to simulated data points. The step width in Θ is 5°, and 0.02 Hz in f

While the symbols and color map are the same as in Fig. 7, we now free ourselves from the restriction of using the steady state as an initial condition for each new driving frequency as done in the experiments. Instead, the driving frequency is now increased in a semi-static way for each shaft angle. After each frequency increase of 0.2 Hz, a waiting time of 1000 rotations is implemented. The starting geometry for each new Θ is $\alpha = 0°$ and $\beta = 180°$.

A striking feature is the symmetry breaking between $\Theta = -30°$ and $\Theta = 30°$ above $f = 20$ Hz. This can be explained by our starting configuration, which breaks the mirror symmetry between positive and negative Θ values. Moreover, it clearly indicates that multi-stability is present in this regime.

Outside the immediate surrounding of the cogging-free shaft angle configurations, e. g. at $\Theta = 25°$, a maximum of RMS_δ is seen near $f = 1.25$ Hz. For further increase in driving frequency, the amplitude decreases but forms a second maximum at $f \approx 2.5$ Hz. This marks a window of T-periodic response of the output in an otherwise $T/2$-periodic surrounding and can be seen in detail in Fig. 9.

If f is increased even further, RMS_δ remains small until a certain frequency threshold. Beyond that, the input is no longer locked to the output, the output rather slips through. A more detailed investigation of this transition is shown in Fig. 10.

An interesting feature of Fig. 8 is the transition from $T/2$ periodicity to T periodicity, occurring e. g. at $\Theta = 25\,°$ near $f = 2.2$ Hz. This period-doubling transition is examined in detail in Fig. 9. We simulated this transition by changing the driving frequency in a quasi-static manner, i. e., after every frequency change the simulation of (22) was allowed to relax into an equilibrium situation. This protocol was applied both for increasing and decreasing frequency steps to cope with the hysteresis in this transition.

In the bottom panel of Fig. 9, the reciprocal of the total harmonic distortion $\mathrm{THD}_\mathrm{F}^{-1}$ is shown. Its values are effectively zero below 1.8 Hz and above 2.5 Hz. In between these frequencies, we see a drastic change toward finite values of $\mathrm{THD}_\mathrm{F}^{-1}$ that reach a maximum around 2.1 Hz. Hysteresis is clearly present from 1.9 Hz to 2.5 Hz, between increasing and decreasing driving frequencies. At 2.5 Hz as small deviation between the increasing and decreasing branch can also be observed. This is presumably caused by the critical slowing down of the dynamics near this period-doubling bifurcation.

The middle panel shows δ_fund, the fundamental mode of the discrete Fourier transform of the angle difference $\delta(t)$. Its values are zero where $\mathrm{THD}_\mathrm{F}^{-1}$ is zero, and they are finite in the same regime as well. However, for decreasing driving frequencies, δ_fund reaches its maximum at a lower f than $\mathrm{THD}_\mathrm{F}^{-1}$ at about 1.9 Hz. This plot is especially well-suited to illustrate that we are dealing with a supercritical period-doubling bifurcation at 2.5 Hz with the characteristic square root increase in the order parameter δ_fund. The bifurcation at 2.1 Hz is subcritical, on the other hand. Its unstable branch gains stability in a saddle-node bifurcation at 1.85 Hz [19].

The two insets in the middle panel show the trajectories of $\beta(\alpha)$ and the corresponding magnetic field energy

$$E(\alpha, \beta) = \frac{\mu_0}{4\pi} \frac{m_1 m_2}{r^3} \left(\sin\alpha \sin\beta + \Delta \cos\alpha \cos\beta\right) \tag{25}$$

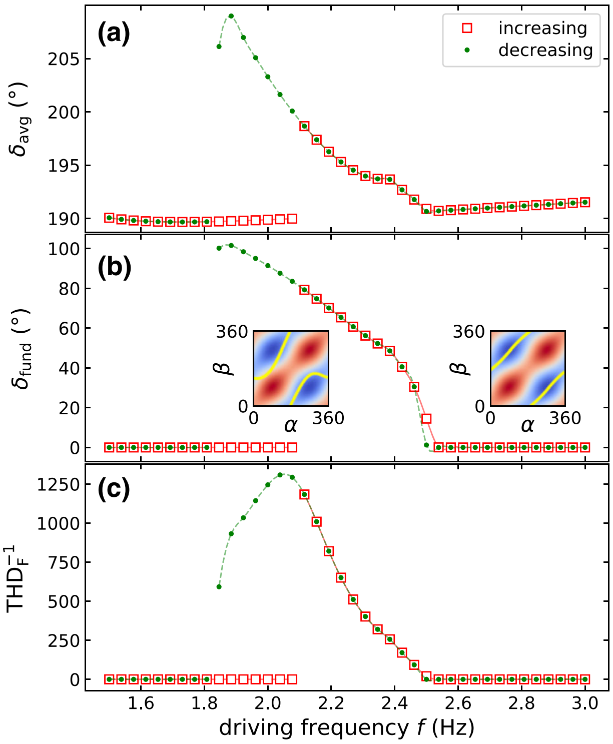

Fig. 9 Numerical simulation of the transition between T-periodic response and $T/2$ periodicity for increasing (open squares) and decreasing (solid circles) driving frequencies ($\Theta = 25°$). The connecting lines are guides to the eye. The left inset shows a T-periodic phase trajectory at $f = 2.1$ Hz, the right inset a $T/2$-periodic trajectory at $f = 2.7$ Hz. The background color of the insets indicates the strength of the magnetic field energy (valleys in blue, hills in red)

of the output dipole $\mathbf{m}_2$ in the field of the input dipole $\mathbf{m}_1$, color coded in the background. The left inset was taken for decreasing frequencies at $f = 2.1$ Hz. The evolution in the range $0° - 180°$ of $\beta(\alpha)$ is substantially different from the evolution in the range $180° - 360°$, a clear manifestation of T periodicity.

The right inset shows the behavior for decreasing frequency steps at $f = 2.7$ Hz. The trajectory is now similar in the first and the second half of the driving cycle, a clear indication of $T/2$ periodicity.

The top panel shows the calculated value δ_{avg} averaged over one full rotation of the input. It measures the average lag between the output and the input angle. The hysteresis also finds a manifestation in this lag. δ_{avg} slightly increases with an increase in driving frequency for $f > 2.5$ Hz. This is due to the increased damping caused by the liquid-like friction. Below 1.8 Hz, one can observe a local minimum of δ_{avg}. We cannot provide a simple explanation for this minimum, but it might be connected to the resonance phenomenon near 1.25 Hz, mentioned in the discussion of Fig. 8.

Fig. 8 clearly indicates that the output of the gear might slip through for any Θ, provided that the driving frequency is large enough. Understanding the nature of this transition is of greatest technological interest for the practical application of the gear. Thus, we simulated this transition by applying the same procedure used to calculate Fig. 9. The results for $\Theta = 0°$, the fundamental cogging-free coupling geometry, are presented in Fig. 10. Starting at a small driving frequency of 1 Hz, the output is locked to the input in the sense that a constant angle difference δ is asymptotically achieved. This locked state is illustrated by the yellow line in the upper inset of Fig. 10, which yields from a simulation at a driving frequency of 6 Hz. The background color of the inset indicates the strength of the magnetic field energy given by (25). In the locked state, the yellow trajectory remains in the valley of the minimal energy configuration indicated in blue. Increasing the driving frequency leads to an increase in the locked angle according to

$$\delta_{\text{lock}} = \arcsin\left(\frac{\zeta\dot{\beta} + \eta}{g_\tau}\right) + 180°, \tag{26}$$

which is determined from (22) by assuming $\ddot{\beta} = 0$.

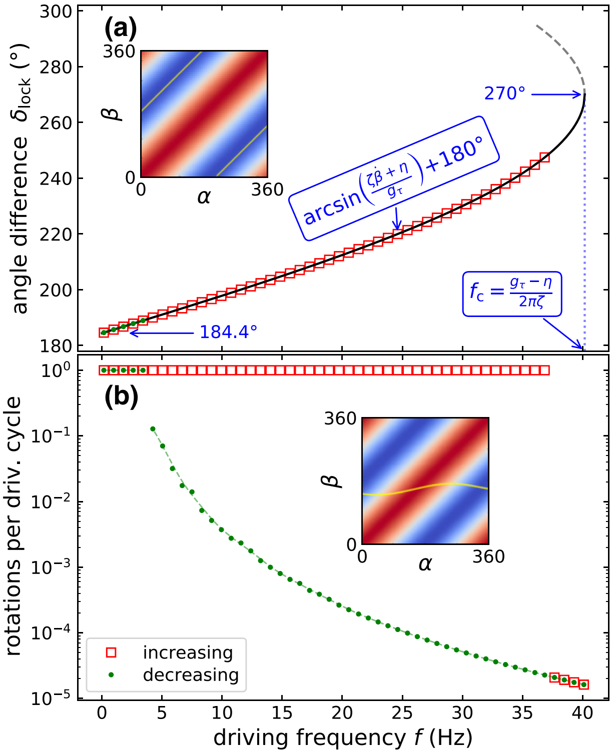

Fig. 10 Numerical simulation of the transition between the locked and unlocked operation mode for increasing (open squares) and decreasing (solid circles) driving frequencies. **a** shows the locked state, together with the stable (black line) and unstable (dashed gray line) branch of its analytical solution. **b** shows the slip-through state, where the dashed green line is a guide to the eye. The insets both show a phase trajectory at 6 Hz., with the same coding used as in Fig. 9

The locked branch starts at a finite value of 184.4° determined by the solid state friction for a driving frequency $f \to 0$ Hz. The branch terminates in a saddle node bifurcation a value of 270° for a driving frequency $f_\mathrm{c} = \frac{g_\tau - \eta}{2\pi\zeta}$ determined by both friction coefficients. It is interesting to note that the numerical simulation of this branch loses stability slightly before reaching the saddle node bifurcation located at 270°. This can be explained by the distortion caused by the finite frequency steps of about 1 Hz in the numerical simulation.

In the unlocked slip-through state, which is reached after a transient following the instability of the locked state, the output almost ceases to move expect for a relatively small wiggling. The lower inset provides an example for the phase trajectory at a driving frequency of 6 Hz. At this frequency, a clear back and forth movement of the output can be seen, while the net rotation frequency determined by the difference $\beta(360°) - \beta(0°)$ is less than 1 % of the driving frequency and thus barely visible. This net rotation frequency is indicated by the solid green circles in Fig. 10b. Decreasing the driving frequency leads to an increase in this slow rotation. The slip through branch terminates near 5 Hz, i.e., the width of the hysteresis spans over 80 % of the width of the locked state. For most technical applications, this hysteresis would presumably have to be avoided. This is done by working below that critical frequency, namely 5 Hz in our case. This frequency could be increased by using a stronger magnetic coupling g_τ.

5 Conclusion and outlook

In this work, the dynamic response of a particular magnetic gear based on pure dipole-dipole coupling is analyzed experimentally for the first time. A mathematical model for the dynamics of the output shaft is proposed, which includes two types of friction in the bearing. This simplified model describes the experimental findings on a semi-quantitative level. In particular, it can reproduce T periodicity, $T/2$ periodicity, and chaotic responses. Moreover, it enables us to understand the nature of the bifurcations between these different states. Most importantly, it helps us to clarify the parameter range for a safe operation of this magnetic gear: The driving frequency needs to be sufficiently low, and shaft angles need to be sufficiently far from $\Theta = 35.26°$, the angle where the output rotation changes its sign.

The mathematical model revealed $3T$ periodicity in a small parameter range, which has not been seen in the experiment. Understanding this discrepancy is the goal of ongoing work.

Acknowledgements It is a pleasure to thank R. Richter, W. Schöpf, and S. Völkel for valuable hints and discussions.

Open Access This article is licensed under a Creative Commons Attribution 4.0 International License, which permits use, sharing, adaptation, distribution and reproduction in any medium or format, as long as you give appropriate credit to the original author(s) and the source, provide a link to the Creative Commons licence, and indicate if changes were made. The images or other third party material in this article are included in the article's Creative Commons licence, unless indicated otherwise in a credit line to the material. If material is not included in the article's Creative Commons licence and your intended use is not permitted by statutory regulation or exceeds the permitted use, you will need to obtain permission directly from the copyright holder. To view a copy of this licence, visit http://creativecommons.org/licenses/by/4.0/.

Funding Open Access funding enabled and organized by Projekt DEAL. This work has been supported by the Deutsche Forschungsgemeinschaft (DFG) - Project No. 389197450.

Compliance with ethical standards

Conflict of interest On behalf of all authors, the corresponding author states that there is no conflict of interest.

References

1. Furlani, E.P.: Permanent Magnet and Electromechanical Devices. Electromagnetism, pp. 207–333. Academic Press, San Diego (2001). https://doi.org/10.1016/B978-012269951-1/50005-X
2. Tsurumoto, K., Kikuchi, S.: A new magnetic gear using permanent magnet. IEEE Trans. Magn. **23**, 3622 (1987)
3. Wang, L., Shen, J.X., Luk, P.C.K., Fei, W.Z., Wang, C., Hao, H.: Development of a magnetic-geared permanent-magnet brushless motor. IEEE Trans. Magn. **45**(10), 4578 (2009)
4. Jian, L., Chau, K., Jiang, J.: A magnetic-geared outer-rotor permanent-magnet brushless machine for wind power generation. IEEE Trans. Ind. Appl. **45**(3), 954 (2009)
5. Atallah, K., Howe, D.: A novel high-performance magnetic gear. IEEE Trans. Magn. **37**(4), 2844 (2001)
6. Park, E.J., Jung, S.Y., Kim, Y.J.: Comparison of magnetic gear characteristics using different permanent magnet materials. IEEE Trans. Appl. Supercond. **30**(4), 1 (2020)
7. Schönke, J.: Smooth teeth: why multipoles are perfect gears. Phys. Rev. Appl. **4**, 064007 (2015). https://doi.org/10.1103/PhysRevApplied.4.064007
8. Schönke, J., Schneider, T.M., Rehberg, I.: Infinite geometric frustration in a cubic dipole cluster. Phys. Rev. B **91**, 020410 (2015). https://doi.org/10.1103/PhysRevB.91.020410
9. Hartung, S., Sommer, F., Völkel, S., Schönke, J., Rehberg, I.: Assembly of eight spherical magnets into a dotriacontapole configuration. Phys. Rev. B **98**, 214424 (2018). https://doi.org/10.1103/PhysRevB.98.214424
10. Borgers, S., Völkel, S., Schöpf, W., Rehberg, I.: Exploring cogging free magnetic gears. Am. J. Phys. **86**(6), 460 (2018)
11. Kugellager-express-gmbh. https://www.kugellager-express.de/full-ceramic-deep-groove-ball-bearing-ce-6006-open-30x55x13-mm. Accessed: 2020-05-30
12. Metamotionc - mbientlab. https://mbientlab.com/metamotionc/. Accessed: 2020-05-30
13. Bhushan, B., Sibley, L.B.: Silicon nitride rolling bearings for extreme operating conditions. ASLE Trans. **25**(4), 417 (1982)
14. Wang, L., Snidle, R., Gu, L.: Rolling contact silicon nitride bearing technology: a review of recent research. Wear **246**(1–2), 159 (2000)
15. Dalal, H., Chiu, Y., Rabinowicz, E.: Evaluation of hot pressed silicon nitride as a rolling bearing material. ASLE Trans. **18**(3), 211 (1975)
16. Aramaki, H., Shoda, Y., Morishita, Y., Sawamoto, T.: The performance of ball bearings with silicon nitride ceramic balls in high speed spindles for machine tools. J. Tribol. **110**(4), 693 (1988)
17. Shmilovitz, D.: On the definition of total harmonic distortion and its effect on measurement interpretation. IEEE Trans. Power Deliv. **20**(1), 526 (2005)
18. Haugen, P.T., Edwards, B.F.: Dynamics of two freely rotating dipoles. Am. J. Phys. **88**(5), 365 (2020)
19. Strogatz, S.H.: Nonlinear Dynamics and Chaos. Addison-Wesley, Reading (1994)

Publisher's Note Springer Nature remains neutral with regard to jurisdictional claims in published maps and institutional affiliations.

Acknowledgments

First of all, I thank my advisor, Prof. Dr. Ingo Rehberg, for the kind admission to the EPV chair, the opportunity to work on this project and his great supervision. With his eager support on every topic he created an ideal, goal-focused work environment while always keeping an open ear for all work-related and non-work-related issues.

I thank all of the EPV staff and its students for the friendly atmosphere and its huge support. Especially, I want to thank

- PD Dr. Reinhard Richter for his helpful, stimulating ideas and comments in our weekly group meetings and his great company when working on common topics and in the time in-between.
- Dr. Wolfgang Schöpf for his helpful comments on my work in our weekly group meetings, the great advice for my poster presentations, and for always cheering up my mood.
- Simeon Völkel for his witty and intelligent ideas in fruitful discussions around my work and for brightening up the daily life in the laboratory as a great office neighbor and friend.
- Klaus Oetter for his quick and flawless help with all mechanical challenges of my experimental setups and his organization of the “Aktivpause”.
- Andreas Forster for his help with administrative and electronic challenges around my work.
- Christine Linser for her great support and guidance in all organizational regards and her kind spirit.

I thank my parents, Ute and Miloslav, who gave me all they had and more than I ever needed throughout my whole life. Their financial and mental support enabled me to study physics in the first place and eventually come this far.

Finally, I thank my dear wife Hanna for her unconditional encouragement and understanding that let me maintain a positive mindset even in the most stressful times.

Eidesstattliche Versicherung

Hiermit versichere ich an Eides statt, dass ich die vorliegende Arbeit selbstständig verfasst und keine anderen als die von mir angegebenen Quellen und Hilfsmittel verwendet habe.

Weiterhin erkläre ich, dass ich die Hilfe von gewerblichen Promotionsberatern bzw. -vermittlern oder ähnlichen Dienstleistern weder bisher in Anspruch genommen habe, noch künftig in Anspruch nehmen werde.

Zusätzlich erkläre ich hiermit, dass ich keinerlei frühere Promotionsversuche unternommen habe.

Bayreuth, den 30. August 2021 ....
Stefan Hartung